Agricultural and Forest Meteorology 369 (2025) 110570

Contents lists available at ScienceDirect

Agricultural and Forest Meteorology

journal homepage: www.elsevier.com/locate/agrformet

Surface energy exchanges and stability conditions associated with convective intense rainfall events on the central Andes of Peru

José Luis Flores-Rojas [a,*], David A. Guizado-Vidal [a], Jairo Valdivia-Prado [a], Yamina Silva [a], Elver Villalobos-Puma [c], Luis Suárez-Salas [a], Zenón Mata-Adauto [b], Hugo Abi Karam [d]

[a] Instituto Geofísico del Peru, Calle Badajoz 169 Urb. Mayorazgo IV Etapa. Ate, Lima 15012, Peru
[b] Universidad Nacional del Centro del Perú. Facultad de Agronomia., Av. Mariscal Castilla 3909, Huancayo, Junín, Peru
[c] Instituto Nacional de Investigación en Glaciares y Ecosistemas de Montaña, Jr. Juan Bautista Mejía 887 Huaraz, Áncash, Peru
[d] Universidade Federal de Rio de Janeiro, Rio de Janeiro - UFRJ/IGEO/CCMN. Rua Athos da Silveira Ramos, 274, Bloco G1 Cidade Universitária - Ilha do Fundão Rio de Janeiro, RJ, CEP: 21941-916, Brazil

ARTICLE INFO

Keywords:
Convective rainfall events
Surface energy balance
Stability conditions
Model simulations
Mantaro valley

ABSTRACT

This study presents an in-depth analysis of precipitation patterns, surface energy balance (SEB) components, and atmospheric vertical gradients (AVG) in the Huancayo Geophysical Observatory (HYGO) situated in an agricultural region inside the Mantaro valley within the central Andes of Peru, utilizing data from January 2018 to April 2022 and climatic-scale data from 1965 to 2018. Our findings reveal distinct daily and seasonal precipitation patterns, with peak occurrences in the late afternoon and early evening hours, and a pronounced seasonal variation aligning with dry and rainy periods. Analysis of 21 intense precipitation events linked to convective activity offers crucial insights for weather forecasting and disaster preparedness. These events were identified using in situ gauge pluviometers, the MIRA-35c vertical profiler radar and GPM-IMERG rainfall products. The turbulent energy fluxes: sensible (Q_H) and latent (Q_E) were estimated using the aerodynamic flux-gradient method and the ground heat flux to the surface was estimated with the scheme of Foken and Napo. Moreover, the study evaluates the efficacy of the Advanced Regional Prediction System (ARPS) model in analyzing turbulent energy fluxes during these events. A comparison with the bulk aerodynamic method indicated underestimations and overestimations by the ARPS model in predicting Q_H and Q_E, respectively, necessitating focused calibration and updates in satellite-derived data. Key observations include significant increases in Q_E and horizontal momentum flux (τ) before convective precipitation events, marking them as potential precursor variables. Additionally, notable decreases in water vapor mixing ratio vertical gradient (WMVG) and Richardson number (RIN), along with increases in horizontal wind gradient (HWVG), suggest changes in surface moisture fluxes and boundary layer dynamics, crucial for convective rainfall initiation. This comprehensive analysis underscores the importance of understanding atmospheric dynamics for improved prediction and preparedness strategies in the face of climatic variability.

1. Introduction

Atmospheric turbulent fluxes at the land surface govern the energy and mass exchanges among the hydrosphere, atmosphere, and biosphere (Sellers et al., 1986; Su, 2002). These processes significantly shape the thermodynamics and dynamics of the atmospheric boundary layer, influencing surface temperature, humidity, and convection (Thompson et al., 2004; Martínez-Castro et al., 2019; Coutts et al., 2007). Understanding these exchanges is particularly critical in mountainous regions like the Andes, where complex topography interacts with synoptic and mesoscale atmospheric processes to produce intense convective rainfall events (Rouse et al., 2003; Jun et al., 2007; Bhat and Arunchandra, 2008; Xufeng and Mingguo, 2009).

Surface sensible heating, a key factor driving the thermal characteristics of the planetary boundary layer, affects the onset of convection (Keenan et al., 1994, 2000). Consequently, research on the surface energy budget is crucial for understanding thunderstorm dynamics, with studies emphasizing the significance of surface fluxes in thunderstorm convective cycles (Beringer and Tapper, 2000; Keenan et al., 2000; Beringer and Tapper, 2002). The initiation of thunderstorms is

* Corresponding author.
E-mail addresses: jflores@igp.gob.pe (J.L. Flores-Rojas), alejandroguivi@gmail.com (D.A. Guizado-Vidal), jvaldivia@igp.gob.pe (J. Valdivia-Prado), fsilva@igp.gob.pe (Y. Silva), evillalobos@inaigem.gob.pe (E. Villalobos-Puma), lsuarez@igp.gob.pe (L. Suárez-Salas), zmata@uncp.edu.pe (Z. Mata-Adauto), hugo@igeo.ufrj.br (H.A. Karam).

https://doi.org/10.1016/j.agrformet.2025.110570
Received 20 May 2024; Received in revised form 2 April 2025; Accepted 15 April 2025
Available online 26 April 2025

Nomenclature

Q^*	Net all wave irradiance (W m^{-2})
Q_H	Turbulent sensible heat flux (W m^{-2})
Q_E	Turbulent latent heat flux (W m^{-2})
Q_G	Molecular ground heat flux (W m^{-2})
τ	Horizontal momentum flux (m^2 s^{-2})
$\partial T_s/\partial z$	Soil temperature gradient (°C m^{-1})
$PTVG$	Potential temperature vertical gradient (°C m^{-1})
RIN	Richardson number
$WMVG$	Water mixing vertical gradient (g kg^{-1} m^{-1})
$HWVG$	horizontal wind vertical gradient (m s^{-1} m^{-1})
$ARPS$	Advance Regional Prediction System
AVG	Atmospheric vertical gradients
$HYGO$	Huancayo Geophysical Observatory
GPM	Global precipitation measurement
SEB	Surface energy balance components

closely linked to surface energy fluxes, with low-level moisture, conditional instability, and lifting mechanisms being critical factors (Keenan et al., 2000; Satyanarayana et al., 2014). Furthermore, two studies have analyzed variations in surface energy fluxes and their impact on the overall energy budget during thunderstorm and non-thunderstorm days in Ranchi, India (Tyagi and Satyanarayana, 2015; Tyagi et al., 2012). These studies aim to provide insights into the fluctuations of surface energy fluxes and their influence on Ranchi's energy balance during different weather conditions.

In the central Andes of Peru, the most intense precipitation events have been observed during late afternoons and early evenings, coinciding with the convergence of thermally driven moisture fluxes originating from both the Pacific Ocean and the Amazon Basin (Garreaud, 1999; Junquas et al., 2018). Furthermore, these robust moisture convergence patterns are primarily triggered by the interaction between thermally induced westerly winds, coupled with mid and upper-level westerly circulations, and thermally induced easterly winds. These complex atmospheric dynamics result in the formation of severe thunderstorms within the Mantaro Valley during the afternoon hours (Flores-Rojas et al., 2021; Villalobos-Puma et al., 2020).

Moreover, during a field campaign conducted between 2017 and 2018 at the Huancayo Geophysical Observatory (HYGO) in the central Andes of Peru, an analysis of atmospheric dynamics revealed that intense rainfall events were consistently linked to thermal meso-scale circulations. These circulations facilitated the transportation of moisture fluxes through passes with gentle slopes along both sides of the Andes. At the synoptic scale, these rainfall events could be classified into two distinct groups: one associated with westerly circulations (WC) and the other with easterly circulations (EC) in the mid and upper levels of the atmosphere (Flores-Rojas et al., 2020).

On the other hand, in a study conducted by Flores-Rojas et al. (2019a), an extensive analysis of daily and monthly variations pertaining to the surface boundary layer and surface energy balance was carried out within a sparsely vegetated canopy at the HYGO. This analysis involved a comparison of sensible heat flux (Q_H) and latent heat flux (Q_E), which were estimated using both the aerodynamic method and the Bowen-ratio energy-balance method. Impressively, the results of this comparison exhibited a high level of agreement, with an R^2 value exceeding 0.8. Additionally, when comparing the available energy with the sum of Q_E and Q_H fluxes, a substantial level of agreement was observed, as indicated by an R^2 value of 0.86. Notably, this agreement was maintained despite significant imbalances occurring after sunrise and around noon. These imbalances are likely attributable to advection processes triggered by surface heterogeneities surrounding the HYGO site, potentially exacerbated by the mountain-valley circulation phenomenon. In addition, Callanaupa et al. (2021) conducted a pioneering study on evapotranspiration mechanisms in the high central Peruvian Andes, where understanding was limited. This study used an eddy covariance system at the HYGO by documenting hourly, daily, and monthly variations in surface energy fluxes from July 2016 to June 2017. Its results revealed that evapotranspiration in this region is influenced by water and energy limitations during the wet and dry seasons, respectively. In the wet season (January–March), latent heat flux (Q_E) dominated over sensible heat flux (Q_H), primarily driven by incoming solar radiation, resulting in a daily mean evapotranspiration of 3.45 mm. In contrast, the dry season (June–August) exhibited higher Q_H, with a daily mean evapotranspiration of 0.95 mm.

However, these previous studies have primarily focused on observational data, with limited exploration of the dynamic interactions between surface energy exchanges, boundary layer dynamics, and convective precipitation processes. To address these gaps, this study undertakes a comprehensive analysis of precipitation dynamics, surface energy balance (SEB) components, and atmospheric stability conditions. The overarching aim is to deepen the understanding of how surface-atmosphere interactions drive intense convective rainfall in the central Andes. Specifically, the objectives are the following: (1) Characterization of precipitation patterns by analyzing the daily and seasonal variations of precipitation using long-term data (1965–2018). (2) Characterization event-specific observations (2018–2022) and investigation of temporal variability of intense rainfall events using high resolution (one minute) data. (3) Examination of surface energy exchanges by quantifying the components of the SEB (Q^*, Q_H, Q_E, Q_G) under varying atmospheric stability conditions and assessing how variations in SEB components influence boundary layer dynamics and the initiation of convective processes. (4) Identifying atmospheric precursors to convective rainfall by analyzing changes in vertical gradients of water vapor mixing ratio (WMVG), horizontal wind gradient (HWVG), and Richardson number (RIN) preceding rainfall events and determining the role of these variables as early indicators of intense precipitation. (5) Comparison between the SEB components during intense rainfall and non-intense rainfall conditions to identify the variables that can be used as precursor signals for the occurrence of convective rainfall activity. (6) Evaluation of model performance by assessing the ability of the Advanced Regional Prediction System (ARPS) to simulate turbulent fluxes and convective rainfall events. This includes developing calibration strategies for both the ARPS model and satellite-derived datasets, with the aim of improving the accuracy of sensible heat flux (Q_H) and latent heat flux (Q_E) predictions. (7) Exploration implications for disaster preparedness by investigation into how the previous findings can inform early warning systems and enhance forecasting capabilities for extreme weather events in mountainous regions.

This research not only enhances the understanding of atmospheric dynamics in the Andes but also contributes to global efforts aimed at improving weather prediction and mitigating the impacts of climate variability on vulnerable populations. Section 2 provides an overview of the key characteristics of the study site, focusing on the location and unique features of the Huancayo Geophysical Observatory (HYGO). Section 3 details the instruments utilized in this study, emphasizing their capabilities and relevance to the research objectives. Section 4 outlines the methodological framework, describing the processes and techniques applied to ensure robust and reliable findings. Sections 5 and 6 present the primary results of the study, along with an in-depth discussion of their implications and relevance. Finally, Section 7 synthesizes the outcomes, offering a concise conclusion that highlights the contributions and broader significance of this research.

2. Site and location

The HYGO is located in the Mantaro River Basin, central Peruvian Andes and is characterized by its high-altitude setting, uni-modal

Table 1
Summary of key site and location characteristics at the HYGO in the Mantaro River Basin, central Peruvian Andes. The table highlights geographic, climatic, and environmental factors, along with referenced findings from recent studies on precipitation, temperature patterns, evapo-transpiration, and atmospheric conditions.

Characteristics	Description	References
Location Coordinates (HYGO)	12.04° S, 75.32° W	Fig. 1a (IGP)
Elevation (HYGO)	3350 masl	Fig. 1a (IGP)
Drainage Area (MRB)	34 550 km^2	Fig. 1b,c (IGP)
Altitude Range (MRB)	500 to 5300 masl	Fig. 1b,c (IGP)
Mean Altitude (MRB)	3870 masl	Fig. 1b,c (IGP)
Proximity to Mantaro River	7 km	Fig. 1d (IGP)
Proximity to Huancayo City	12 km	Fig. 1d (IGP)
Seasons	Uni-modal seasonalprecipitation cycle	Silva et al. (2008) and Espinoza-Villar et al. (2009)
Dry Season Period	April to August	Silva et al. (2008) and Espinoza-Villar et al. (2009)
Rainy Season Period	September to March	Silva et al. (2008) and Espinoza-Villar et al. (2009)
Peak Rainfall Period	January to March	Silva et al. (2008) and Espinoza-Villar et al. (2009)
Annual Rainfall Contribution (Rainy Season)	83% of accumulatedannual rainfall	Silva et al. (2010)

precipitation pattern, and distinct seasonal evapotranspiration dynamics. Detailed geographic, climatic, and environmental features are summarized in Table 1 and the main geographical characteristics are showed in Fig. 1.

In addition, it is important to emphasize that the daily and monthly variations of the surface boundary layer within the sparsely vegetated canopy of HYGO throughout a year (May 2018-April 2019) reveal distinct temperature and atmospheric stability patterns. June and July exhibit the lowest mean monthly temperatures and more stable conditions before sunrise, whereas October and November experience the highest mean monthly temperatures and increased atmospheric instability in February and March. From May to August, inverted water vapor profiles near the surface are prevalent, particularly in July, indicating the transfer of water vapor as dewfall. Wind direction patterns reveal well-defined mountain–valley circulation, predominantly from south-east to south-west, especially during the fall and winter months (April–August). The maximum mean monthly sensible heat fluxes (Q_H) are observed in June and September, while February and March exhibit the minimum values. Conversely, maximum mean monthly latent heat fluxes (Q_E) occur in February and March, with minimum values in June and July (Flores-Rojas et al., 2019a).

Furthermore, a recent study by Callanaupa et al. (2021) underscores that evapotranspiration over the high central Peruvian Andes is influenced by water and energy limitations during the dry and wet seasons, respectively. In the wet season (January–March), latent heat flux (Q_E) surpasses sensible heat flux (Q_H), with daily evapotranspiration variability primarily linked to incoming solar radiation, averaging 3.45 mm per day. In contrast, the dry season (June–August) exhibits greater Q_H values, resulting in a daily mean evapotranspiration of 0.95 mm. Additionally, evapotranspiration exhibits a significant correlation with daily soil moisture variability.

3. Instrumentation

3.1. Sensors

Table 2 outlines the main instruments at the Laboratory of Physics, Microphysics, and Radiation (LAMAR) in the Huancayo Geophysical Observatory (HYGO). It details their measurements, technologies, and installation setups which are showed in Fig. 2. Instruments include rain gauge sensor, air temperature and humidity probes, wind sensors, soil heat flux plates, tensiometers for soil moisture and temperature, and radiative sensors (pyranometers, pyrheliometers, and pyrgeometers). These devices, installed on gradient and radiation towers, enable high-precision monitoring of atmospheric, soil, and radiative properties critical for environmental research (Flores-Rojas et al., 2019a, 2021).

Table 2
Summary of the main instruments used at the Laboratory of Physics, Microphysics, and Radiation (LAMAR) in the HYGO. The table includes details on the instruments measurements, underlying technologies, and installation setups, highlighting their role in capturing atmospheric, soil, and radiative properties with high precision.

Instrument	Measurement	Technology	Installation
CS700	Rain Gauge with 8 in. Orifice	Campbell Scientific	Meteorological Automatic Station
HMP60 Probe	Air temperature and relative humidity	Campbell Scientific	Gradient tower (30 m high)
03002 Wind Sentry Set	Wind speed and direction	Campbell Scientific 3-cup anemometer and vane	Gradient tower (30 m high)
HFP01 Soil Heat Flux Plate	Soil heat flux	Campbell Scientific Heat flux transfer through soil	Gradient tower (30 m high)
Decagon 5TM VMC Tensiometers	Soil temperature and volumetric water content (VWC)	Thermistors and capacitance/ frequency-domain tech	Gradient tower (30 m high)
CMP10 Pyranometer	Shortwave global, diffuse, and reflected irradiance	Kipp & Zonen CMP10	6 m high tower (BSRN station)
CHP1 Pyrheliometer	Direct solar irradiance	Kipp & Zonen CHP1	6 m high tower (BSRN station)
CGR4 Pyrgeometer	Longwave irradiance (incident and emitted)	Kipp & Zonen CGR4	6 m high tower (BSRN station)
2AP Sun Tracker	Diffuse irradiance from the sky (blocks direct solar)	Articulated shading assembly with tracker	6 m high tower (BSRN station)

3.2. The Global Precipitation Measurement (GPM), the MIRA-35c and the Parsivel 2 disdrometer

Table 3 provides a comprehensive overview of the key characteristics, applications, strengths, and limitations of the three primary instruments used in this study: the Global Precipitation Measurement (GPM) system, the MIRA-35c Ka-Band Radar (Fig. 2b), and the PARSIVEL 2 disdrometer. The MIRA-35c radar is particularly suited for high-resolution detection of cloud microphysics and precipitation processes, offering vertical profiling capabilities with exceptional sensitivity. The GPM system leverages satellite observations to deliver global rainfall estimations with fine temporal and spatial resolution, especially effective in diverse topographical regions such as the Andes.

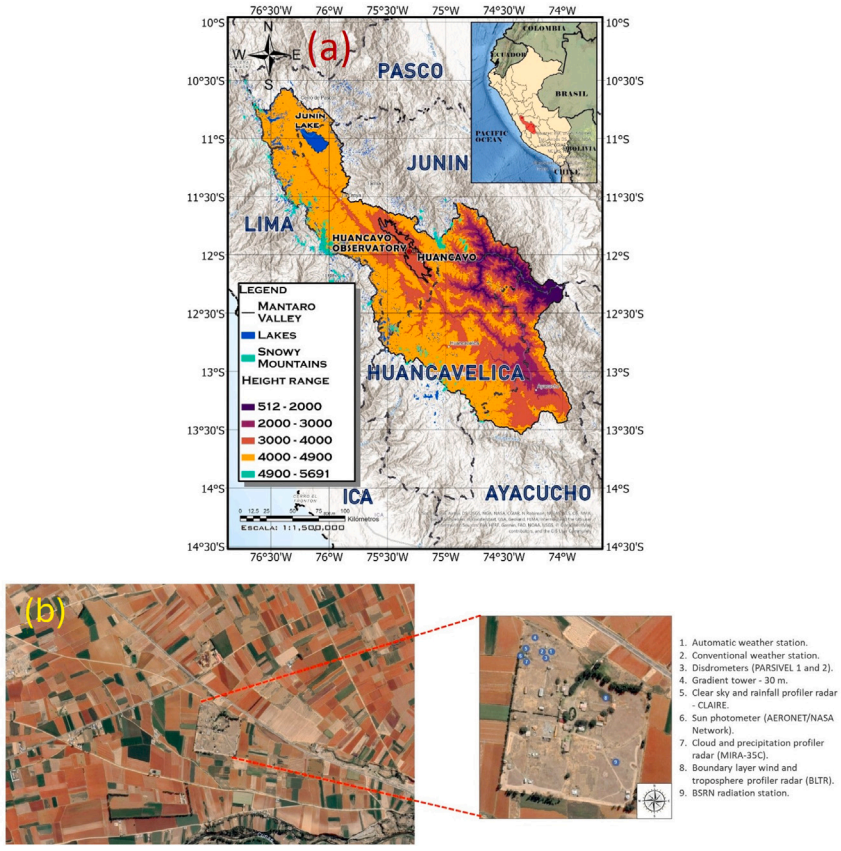

Fig. 1. (a) The location of the HYGO (12.05°S, 75.32°W, 3313 m asl) of the Geophysical Institute of Peru, inside the domain of the Mantaro valley and the Mantaro basin located in the Peruvian Central Andes. (b) Agricultural area around the HYGO and the location of the set of instruments installed in the Laboratory of Atmospheric Microphysics and Radiation (LAMAR).

The PARSIVEL 2 disdrometer complements these systems by providing ground-based measurements of raindrop size distribution and velocity, enabling detailed analyses of precipitation microphysics. Together, these instruments provide a synergistic approach to monitoring and analyzing atmospheric and hydrological phenomena.

4. Methodology

4.1. Estimation of turbulent energy fluxes

In this study, turbulent energy fluxes (sensible and latent) were estimated using flux–gradient methods based on averaged atmospheric profiles and turbulence intensity. Air temperature, relative humidity, wind speed, and direction were measured at six levels on a gradient tower (Fig. 2a). One profile technique was applied—the aerodynamic method (Prueger and Kustas, 2005) based on the Monin–Obukhov similarity theory (Monin and Obukhov, 1954; Monteith and Unsworth, 1990), which assumes that turbulent eddies transport momentum, heat, water vapor, and CO_2 with similar efficiency. The Bulk Richardson number (Ri_B), a nondimensional parameter that characterizes near-surface atmospheric stability by relating buoyant to mechanical forcing, is expressed as follows:

$$\mathbf{Ri}_B = \frac{g}{\overline{T}} \cdot \frac{\Delta\overline{T}/\Delta z}{(\Delta\overline{u}/\Delta z)^2} \tag{1}$$

We assume that low-level changes in wind direction are negligible, so they can be ignored. In Eq. (1), g is the acceleration due to gravity; $overline{T}$ is the mean temperature over a layer of thickness Δz; $\Delta\overline{T}$ and $\Delta\overline{u}$ represent the temperature and wind speed differences, respectively, across this layer. Under neutral stability — typically occurring during early morning or evening on cloudy, windy days — Ri approaches zero. Positive Ri values indicate stable conditions (with cooler surface temperatures relative to higher levels), common during early morning, evening, or overcast periods, while negative Ri_B values signal unstable conditions driven by strong surface heating and enhanced buoyancy. Generally, neutral conditions are infrequent, with unstable and stable states dominating the diurnal cycle (Prueger and Kustas, 2005). The neutral aerodynamic equations for estimating turbulent energy fluxes of momentum (τ), sensible heat (Q_H), and latent heat (Q_E) are thus generalized for stability using Ri_B, as described by Oke (1987) and Arya (1998):

$$\begin{aligned} Q_H &= -C_a k^2 z^2 \left(\frac{\Delta\overline{u}}{\Delta z}\cdot\frac{\Delta\overline{T}}{\Delta z}\right).(\Phi_M\Phi_H)^{-1} \\ Q_E &= -L_v k^2 z^2 \left(\frac{\Delta\overline{u}}{\Delta z}\cdot\frac{\Delta\overline{\rho}_v}{\Delta z}\right).(\Phi_M\Phi_V)^{-1} \\ \tau &= \rho k^2 z^2 \left(\frac{\Delta\overline{u}}{\ln(z_2/z_1)}\right)^2.(\Phi_M\Phi_V)^{-1} \end{aligned} \tag{2}$$

where ρ_v is the water vapor density, estimated from relative humidity, saturation vapor pressure, and air temperature. C_a denotes the heat capacity of air, L_v is the latent heat of vaporization, k is the von Karman's constant (~0.40), and z represents the logarithmic mean height, defined as $(z_2-z_1)/(\ln(z_2/z_1))$. The dimensionless stability functions for momentum, heat, and water vapor — Φ_M, Φ_H and Φ_V, respectively — are expressed as functions of the Richardson number (Arya, 1998).

$$\Phi_M^{-1} = \begin{cases} (1-15\ Ri)^{1/4} & \text{for}\quad Ri<0 \\ (1-5\ Ri) & \text{for}\quad 0<Ri<0.2 \end{cases} \tag{3}$$

$$\Phi_X^{-1} = \begin{cases} (1-15\ Ri)^{1/2} & \text{for}\quad Ri<0 \\ (1-5\ Ri) & \text{for}\quad 0<Ri<0.2 \end{cases}$$

where Φ_X is the appropriate stability function for the property being transferred. Using these functions, it is possible to calculate the

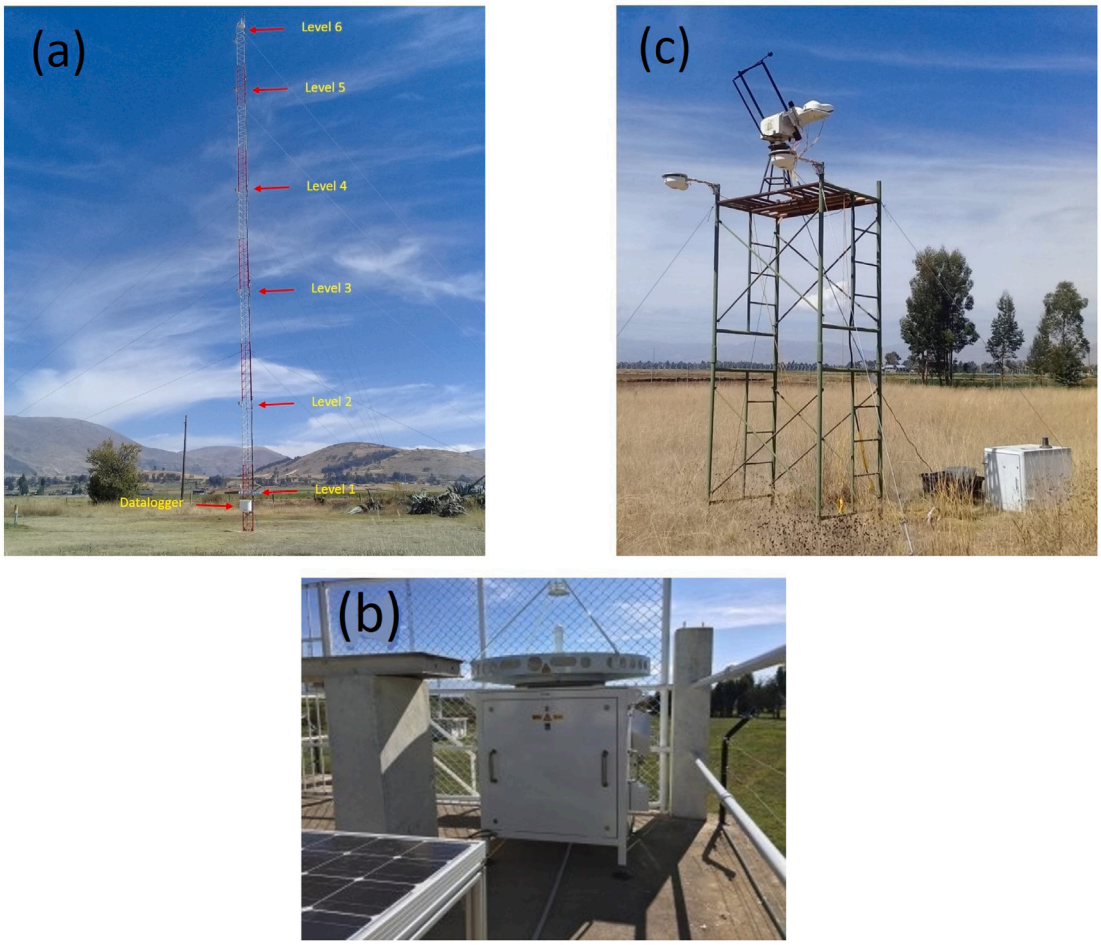

Fig. 2. (a) Gradient tower containing sensors installed at six height levels of 2, 6, 12, 18 24 and 29 m, located in the HYGO. (b) Magnetron-based pulsed Ka-Band Doppler radar MIRA-35c installed in the HYGO. (c) BSRN radiation tower of 6 m high with radiative sensors located in the HYGO.

Table 3
Summary of the key characteristics, applications, strengths, and limitations of the MIRA-35c Ka-Band Radar, Global Precipitation Measurement (GPM) system, and the PARSIVEL 2 disdrometer, highlighting their roles in atmospheric studies.

Feature	MIRA-35c (Ka-Band Radar)	Global Precipitation Measurement (GPM)	Disdrometer (PARSIVEL 2)
Type	Magnetron-based pulsed Ka-band Doppler radar	Joint NASA-JAXA satellite mission	Optical disdrometer (second-generation PARSIVEL 2)
Key Features	Detects Doppler spectra, reflectivity, and linear depolarization ratio (LDR); vertical resolution: 32 m; temporal resolution: 5.3 s; angular opening: 0.6°	Provides rainfall data every 30 min at 0.1° spatial resolution; integrates microwave, infrared, and ground observations	Measures particle size, velocity, and type of precipitation; provides data on drop size distribution and fall velocities
Applications	Detection of clouds, fog, and precipitation; estimation of cloud density and vertical velocity	Monitoring global rainfall; estimation of spatial extent and intensity of rainfall events	Understanding precipitation microphysics; analyzing raindrop characteristics and precipitation intensity
Strengths	High sensitivity; effective for hydrological studies and atmospheric profiling; bridges observational gaps	High accuracy for rainfall estimates; effective for challenging terrains such as the Andes; integrates multiple data sources for improved accuracy	Accurate measurements of drop size distribution (DSD) and velocity; suitable for characterizing precipitation events
Limitations	Requires complex calibration and maintenance; limited spatial coverage	Spatial resolution limited to 0.1°; performance depends on the quality of ground data and calibration algorithms	Susceptible to errors in extreme conditions (e.g., heavy wind); requires regular cleaning and calibration
Additional Information	Effective for detecting microphysical properties of clouds and precipitation; provides critical data for climate studies	IMERG level 3 products outperform other satellite-based rainfall products (e.g., TRMM-TMPA); validated against rain gauge networks globally and in high-altitude regions (e.g., Andes)	Complements radar systems by providing surface-level microphysical data; particularly useful in cross-validation with other precipitation instruments
References	Metek (2015) and Valdivia et al. (2020)	Prakash et al. (2016), Guo et al. (2016), Ma et al. (2016), Tang et al. (2016), Chen (1964), Sharifi et al. (2016), Tan et al. (2016), Hobouchian et al. (2017) and Manz et al. (2017)	OTT Parsivel2 Manual; Relevant microphysical studies

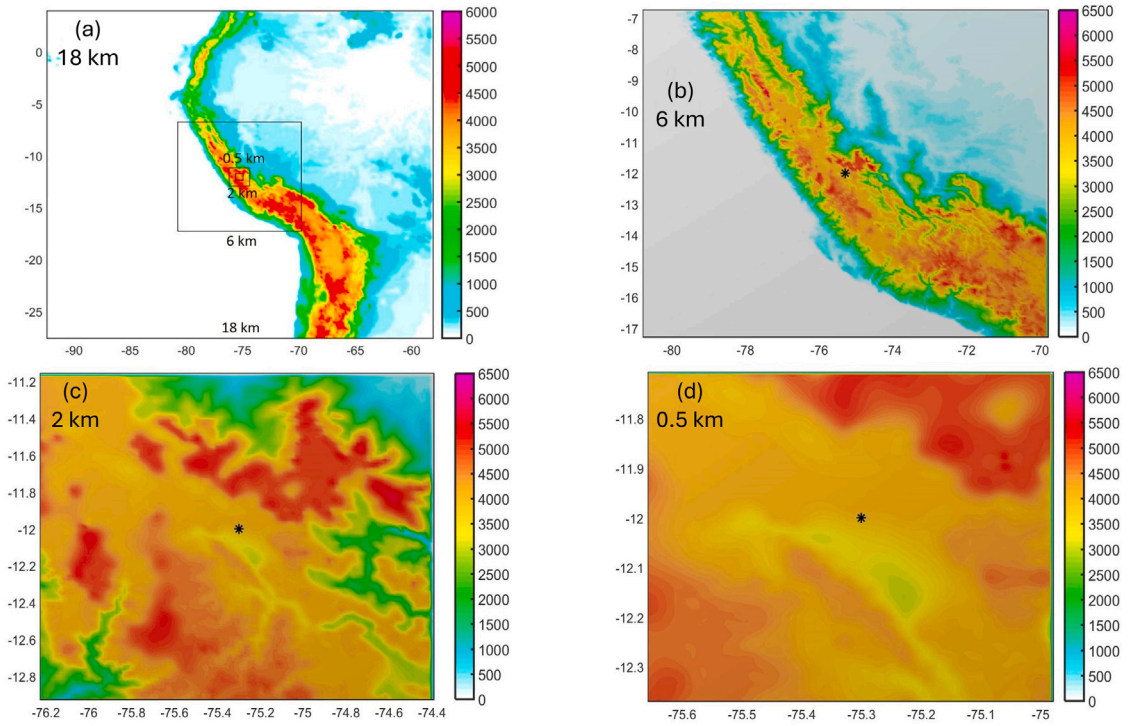

Fig. 3. Topography of the Andes Cordillera illustrating the nested simulation domains configured in the ARPS model, with spatial resolutions of: (a) 18 km, (b) 6 km, (c) 2 km, and (d) 0.5 km. The black mark indicates the location of the HYGO.

combined terms used in Eqs. (2):

$$\begin{cases} (\Phi_M \Phi_X)^{-1} = (1 - 15\ Ri)^{3/4} & \text{for} \quad Ri < 0 \\ (\Phi_M \Phi_X)^{-1} = (1 - 5\ Ri)^{2} & \text{for} \quad 0 < Ri < 0.2 \end{cases} \tag{4}$$

When the atmosphere is neutral (Ri between ±0.01) thermal effects are minimal and only forced convection is present. For conditions of higher instability, buoyancy effects grow in importance through the mixed regime. For values of Ri larger than −1.0, there is weak horizontal motion and strong convective instability. For positive values of Ri close to +0.25 the flow is laminar and vertical mixing is absent.

4.2. Ground heat flux at the surface

During daylight hours, the ground surface and the canopy absorb incoming shortwave radiation, leading to heating. Conversely, during nighttime, the surface cools as a result of the emission of longwave upwelling radiation, causing the surface temperature to drop below that of the air and the deeper soil layers. The available energy, as determined by the net all-wave radiation (Q^*), is partitioned into turbulent sensible (Q_H) and latent (Q_E) heat fluxes, along with the ground heat flux (Q_G), which primarily involves molecular heat transfer. The ground heat flux is proportional to the temperature gradient ($\partial T/\partial z$) and the thermal molecular conductivity a_G expressed in (W m^{-1} K^{-1}). To estimate the ground heat flux at the surface, we combined the soil heat flux measured at a depth of 8 cm using a soil heat flux plate (Fig. 2e) with the heat storage in the layer between the surface and the plate (Foken and Nappo, 2008):

$$Q_G(0) = Q_G(-8\ \text{cm}) + \int_{-z}^{0} C_G(z)\ T(z)\ dz \tag{5}$$

Here, C_G represents the volumetric heat capacity, expressed as $C_G(z) = a_G/\nu_T$, where ν_T is the molecular thermal diffusivity. This parameter can be considered constant with depth when soil moisture is uniform. To implement Eq. (5), we utilized two integrating temperature sensors placed within the soil layer at depths of 2 cm and 5 cm, positioned between the surface and the heat flux plate at 8 cm depth. Consequently, the ground heat flux near the surface can be determined as follows:

$$Q_G(0) = Q_G(-8\ \text{cm}) + \frac{C_G\ |\Delta z|\ |T(t_2) - T(t_1)|}{t_2 - t_1} \tag{6}$$

Moreover, C_G of moist soil at different soil levels were calculated by adding the heat capacity of the dry soil to that of the soil water as follows:

$$C_G = C_d + \theta_V\ \rho_W\ C_W \tag{7}$$

Here, C_d denotes the heat capacity of dry soil, θ_V represents the volumetric soil water content, ρ_W is the density of water (1000 kg m^{-3}), and C_W is the specific heat of water (4.18×10^3 J kg^{-1} K^{-1}). For clay soils, a heat capacity of 1.25×10^6 J m^{-3} K^{-1} is a reasonable value, consistent with the soil characteristics of the HYGO (Garay and Ochoa, 2010). This formulation to estimate Q_G can be found in two recently contributions related with the seasonal and daily variations of the energy balance (Flores-Rojas et al., 2019a) and the analysis of extreme frost events (Flores-Rojas et al., 2021) on the HYGO.

4.3. Numerical simulations

The Advance Regional Prediction System (ARPS 5.3.4) model, developed by the Center for Analysis and Prediction of Storms at Oklahoma University, was utilized for this study. This model incorporates state-of-the-art physics parameterization schemes that play a vital role in explicitly predicting convective storms (Xue et al., 2000). Boundary and initial conditions for the simulations were constructed using the GFS reanalysis data, which has a resolution of 0.5°×0.5°. Four domains were selected, each centered on the HYGO and encompassing the central Andes (Fig. 1b), with horizontal resolutions of 18 km (195 × 195 points), 6 km (195 × 195 points), 2 km (99 × 99 points), and 0.5 km (147 × 147 points) which are shown in Fig. 3. The time steps for these domains were set at 20 s, 10 s, 5 s, and 2 s, respectively. The innermost

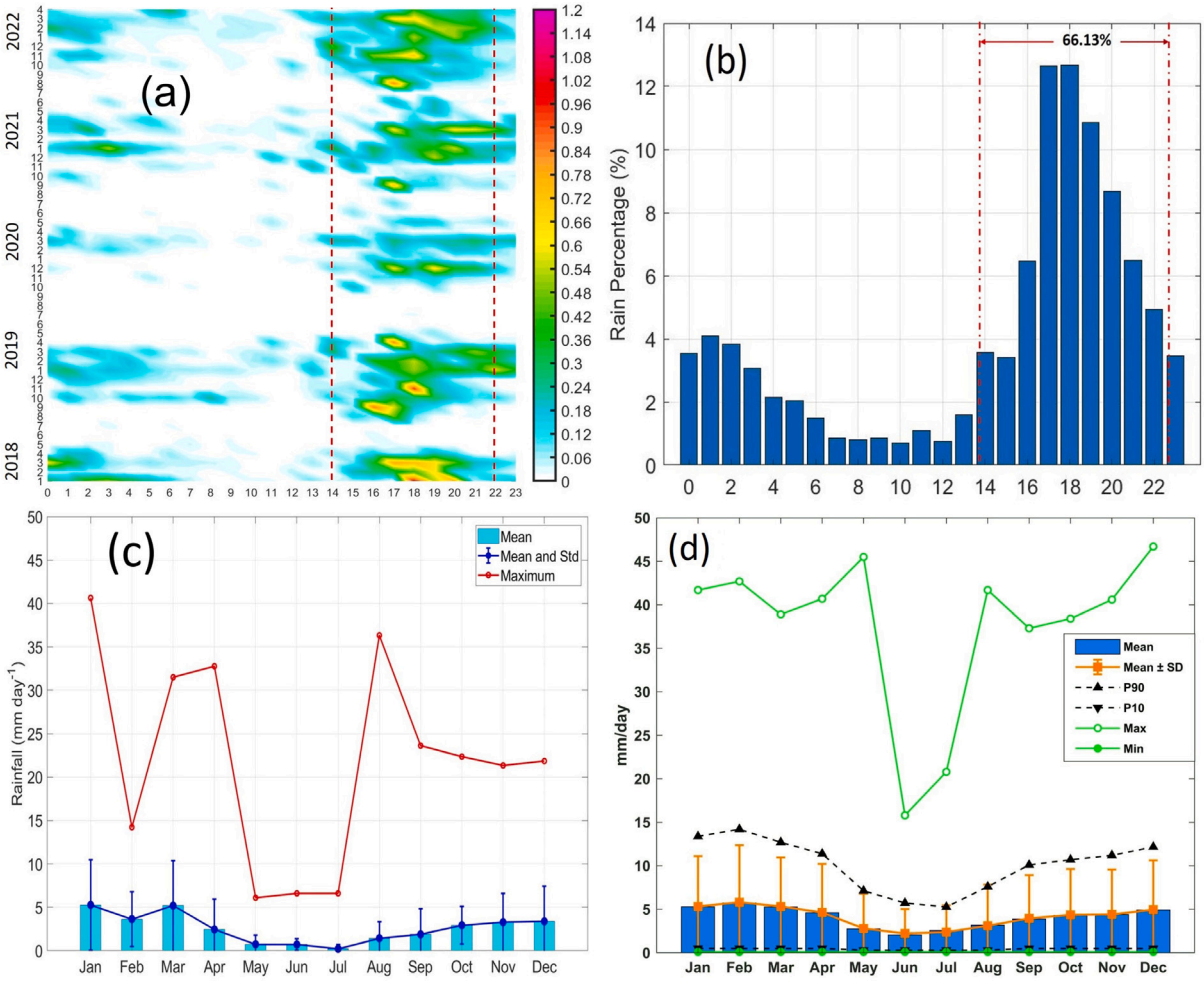

Fig. 4. (a) Daily and seasonal variations of mean hourly accumulated rainfall above the HYGO, between January 2018 and April 2022. The dotted red lines indicate the time period when the greatest amount of rainfall occurred (14 LT - 22 LT). (b) Daily variations of rainfall percentages (%) above the HYGO, during 2018 and March 2020. The dotted red lines highlights that the 66.13% of rainfall occurred between 14 LT and 22 LT. (c) Seasonal cycle of daily accumulated rainfall (mm day^{-1}) between 2018 and 2022 on the HYGO. (d) Seasonal cycle of daily accumulated rainfall (mm day^{-1}) between 1965 and 2018 on the HYGO.

domain had 43 vertical levels on a hyperbolic vertical grid, spanning from 80 m at the bottom to an altitude of 20.5 km.

Turbulent kinetic energy closure scheme of 1.5-order (Xue et al., 2001) was employed to simulate processes within the subgrid boundary layer, while the outer domains utilized the cumulus parameterization of Kain and Fritsch (1993). The ARPS employs a surface-flux scheme that accounts for stability and roughness length, following the methodology proposed by Businger et al. (1971). To enhance computational efficiency in flux calculations, we utilize the procedure introduced by Byun (1990), which relies on exact analytic solutions derived from Monin-Obukhov similarity theory (MOST) and stability parameters expressed in terms of gradient and bulk Richardson numbers for both stable and unstable atmospheric conditions. Additionally, Deardorff (1972b) modifications to Businger's original flux estimation formulation improve the realism of flux predictions, particularly in highly stable or unstable atmospheric conditions. Finally, microphysical processes, including water phase change and precipitation, were simulated using the scheme developed by Schultz (1995). The ARPS simulations commenced at 0000 UTC and ran for 36 h, with a 12-h spin-up period for all domains. Output was recorded at 5 min intervals to capture the high temporal resolutions of thunderstorm scales (Flores-Rojas et al., 2019b, 2020).

5. Results

5.1. Rainfall features on the HYGO

In this section, we conduct an analysis of rainfall data collected using a high-resolution pluviometer (CS700 rain gauge), capturing data at one-minute intervals. Our dataset spans from January 2018 to April 2022. Fig. 4a illustrates the daily and monthly patterns of mean hourly accumulated rainfall above the HYGO. The graph highlights a clearly defined daily precipitation variation, with peak intensities occurring around 1800 local time (LT). Furthermore, our analysis identifies the most intense precipitation events between 14 LT and 22 LT, contrasting with lower rainfall intensities observed between 23 LT and 07 LT. Minimal instances of precipitation are recorded between 07 LT and 14 LT. Notably, the period between 14 LT and 22 LT accounts for a substantial portion, 66.13%, of the total daytime precipitation, as demonstrated in Fig. 4b. This concentration underscores the significance of this time window in terms of rainfall.

Expanding our perspective to encompass the entire study period, from January 2018 to April 2022, the monthly cycle reveals a distinct seasonal pattern in mean hourly accumulated rainfall, as depicted in Fig. 4a. Dry periods are evident from April to August, followed by rainy intervals extending from September to March. This observed pattern aligns with the seasonal variation in daily accumulated rainfall between

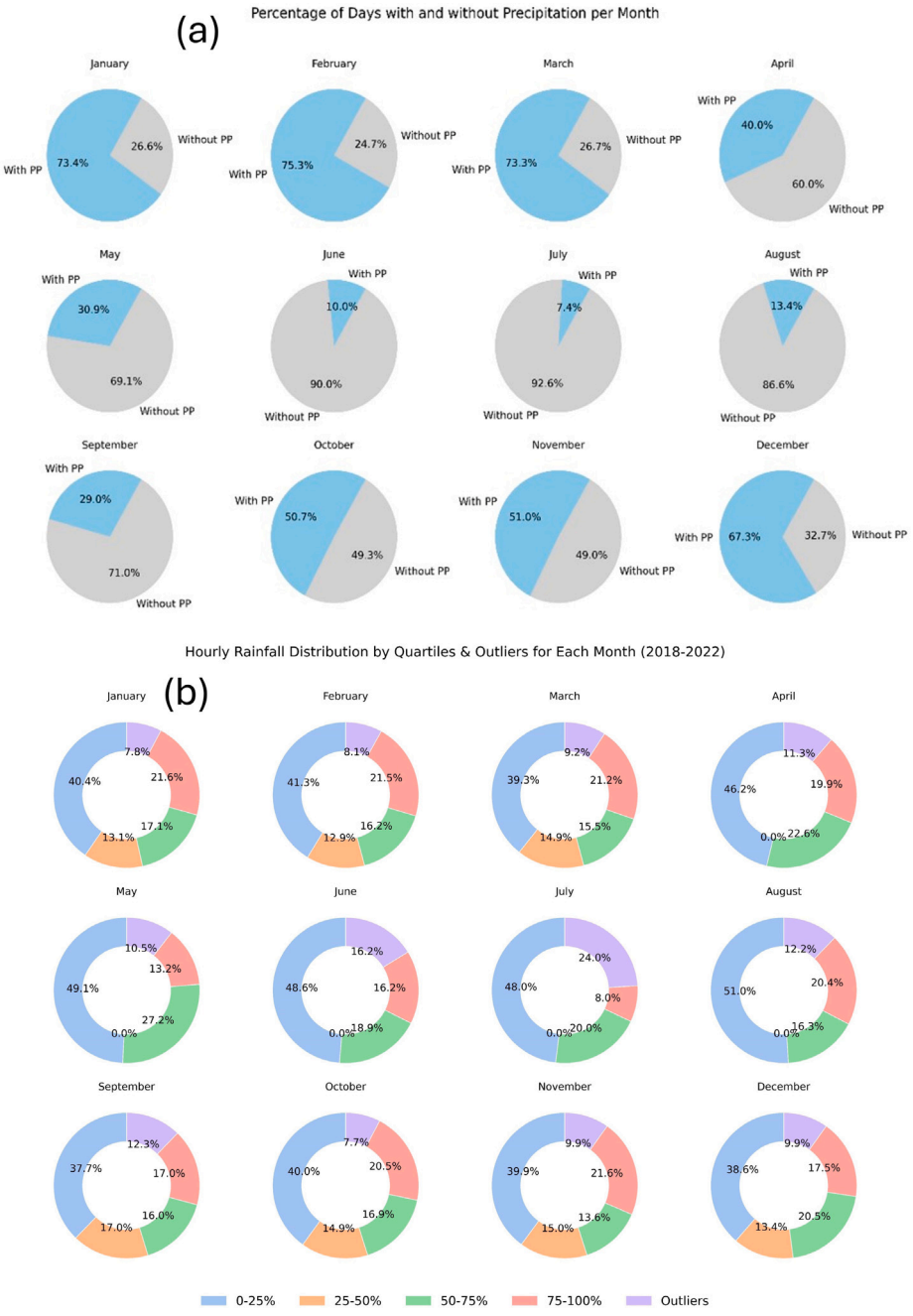

Fig. 5. (a) Pie chart of percentage of days with and without precipitation (mm day^{-1}) above the HYGO and aggregated from 2018 to 2022 and grouped by month. (b) Pie chart of hourly rainfall data (mm h^{-1}) above the HYGO, aggregated from 2018 to 2022, resampled to an hourly basis, grouped by month and excluding zeros. The data were divided into four quartile intervals (0%–25%, 25%–50%, 50%–75%, 75%–100%) for non-outlier values and a separate outlier category. The outliers are higher than $Q_3 + 1.5 \cdot IQR$, where IQR is the interquartile range (Q_3 - Q_1).

2018 and 2022, as shown in Fig. 4c. Here, the highest mean daily accumulated rainfall, approximately 5 mm day^{-1}, occurred between January and March, while the lowest intensities, less than 0.5 mm day^{-1}, are observed from May to July. Intermediate intensities, around 3 mm day^{-1}, characterize the period from August to December. Additionally, Fig. 4c highlights maximum daily accumulated rainfall values, reaching nearly 40 mm day^{-1} during January.

To provide a broader climatic context, Fig. 4d presents the monthly pattern of daily accumulated rainfall (mm day^{-1}) spanning from 1965 to 2018. In agreement with the previous seasonal variation of daily accumulated rainfall between 2018 and 2022, this graph distinctly illustrates a seasonal cycle of precipitation on a climatic scale. The highest intensities are observed from January to March, while the lowest occur from May to July, consistent with the monthly accumulated rainfall data from January 2018 to April 2022 (Fig. 4c).

In this context, Fig. 5a presents the monthly percentage of days with and without precipitation at the HYGO, based on data aggregated from 2018 to 2022. The analysis reveals a pronounced seasonal pattern: precipitation days peak in summer, with February recording 75.3%, and drop to a minimum in winter, with only 7.4% in July. Transitional months exhibit intermediate values, ranging from approximately 40% in April to 50% in October.

Moreover, Fig. 5b shows, hourly rainfall data, aggregated from 2018 to 2022, which were resampled to an hourly basis and grouped by

Fig. 6. Boxplot diagrams with outliers of accumulated hourly precipitation (mm h^{-1}) for each month during the years (a) 2018 (6 events), (b) 2019 (7 events), (c) 2020 (2 events), (d) 2021 (3 events) and (e) 2022 (3 events) occurred on the HYGO. A total of 21 intense rainfall events were identified and are highlighted including the date, time and the amount of precipitation for each one.

month. For each month, the distribution of hourly rainfall was partitioned into five mutually exclusive categories: four quartile intervals (0%–25%, 25%–50%, 50%–75%, and 75%–100% of the non-outlier data) and a separate category for outliers. Outliers were defined using the standard boxplot criteria (values falling outside Q_1 - 1.5 · IQR and Q_3 + 1.5 · IQR). The resulting percentages for each category were visualized as donut charts—each labeled with the full month name. This representation enables a clear comparison of seasonal variability, highlighting both the central tendency of typical rainfall and the frequency of extreme events. For instance, the lower percentage of extreme events were observed during transition months (October: 7.7%), the higher percentage were observed during dry months (July: 24.0%) with intermediate values during summer months (February: 8.1%).

5.2. Identification of intense rainfall events on the HYGO

In this section, we outline a methodological approach for identifying extreme precipitation events associated with convective activity. The process involves the following steps:

1. Boxplot Analysis: We conducted an extensive analysis using boxplots of accumulated hourly precipitation gauge data from the HYGO station, covering the period from August 2018 to April 2022. This analysis, illustrated in Fig. 6, focused on identifying outliers—values that significantly deviate from the typical precipitation range. These outliers serve as key indicators of severe weather conditions, highlighting the occurrence of intense rainfall events.
2. Utilization of Radar Data: We utilized reflectivity and vertical velocity patterns obtained from the MIRA-35c vertical profiler radar (as detailed in Section 3.2), covering the period from August 2018 to April 2022. These remote sensing variables are instrumental in detecting extreme precipitation events associated with convective activity.
3. Remote Sensing Estimation: We employed remote sensing estimates of rainfall from the GPM-IMERG level 3 products (as described in Section 3.2). These products provide global rainfall estimates every 30 min at a resolution of 0.1°, with post-processing corrections based on ground observations. The high spatial–temporal resolution of GPM-IMERG products enables the identification of intense rainfall events at hourly intervals at the HYGO station.

Regarding the boxplot analysis, the most intense hourly precipitation event in 2018 occurred on September 15th at 16:00 local time (LT) with 20.32 mm h^{-1} (Fig. 6a). In 2019, the highest intensity event took place on April 17th at 17:00 LT, registering 21.59 mm h^{-1} (Fig.

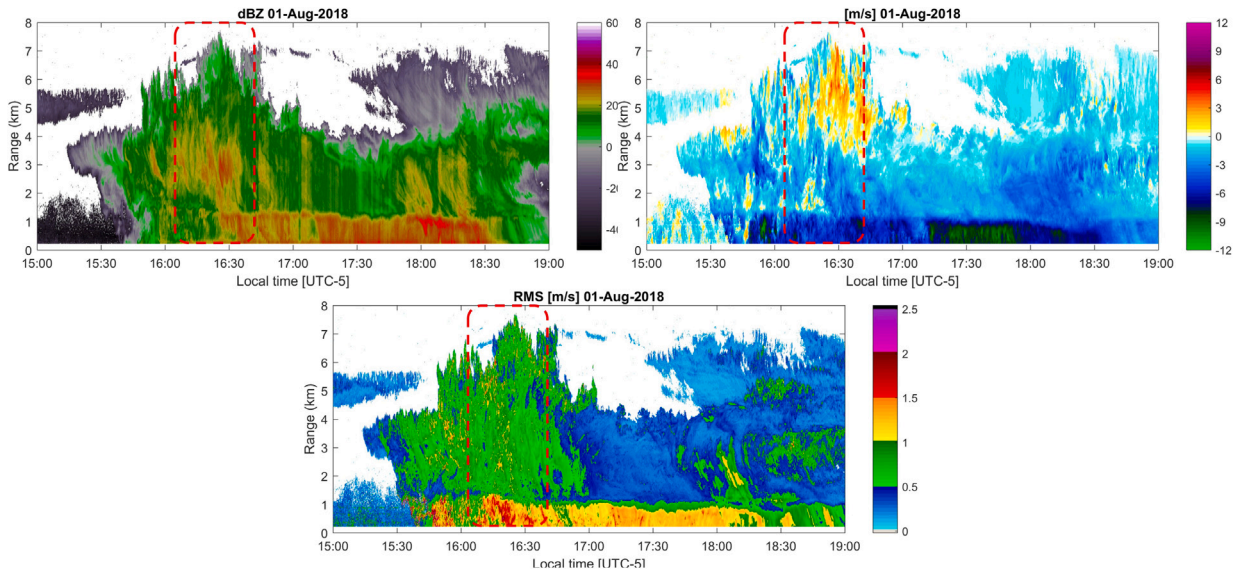

Fig. 7. Time series in local hour (UTC-5) of (a) reflectivity (dBZ), (b) vertical velocity (m s^{-1}), and (c) RMS variable is calculated by taking the square root of the average of the squared values of the radar return. All variables were obtained from the Magnetron-based cloudradar (MIRA-35C) on 01 August 2018 (ETM1).

6b). In 2020, the peak event occurred on September 19th at 17:00 LT, recording 10.67 mm h^{-1} (Fig. 6c). Likewise, in 2021, the most intense event unfolded on August 28th at 17:00 LT, measuring 23.37 mm h^{-1} (Fig. 6d). Up until April 2022, the highest intensity hourly precipitation event occurred on March 14th at 17:00 LT, with a rate of 13.97 mm h^{-1} (Fig. 6e). Notably, the period between 2019 and 2020 experienced a marked decrease in both the frequency and intensity of precipitation events. This decline can be attributed, at least in part, to the presence of a La Niña event, as indicated by the Oceanic Niño Index (ONI). The ONI is widely recognized by NOAA for classifying El Niño (warm) and La Niña (cool) events in the eastern tropical Pacific. The occurrence of La Niña during this period likely played a significant role in driving the observed reduction in intense precipitation events.

Regarding the use of cloud radar MIRA-35C data, Fig. 7a shows the reflectivity measurements during the intense precipitation event on 01 August 2018 (ETM_1). This graphic offers valuable insights into the intensity and spatial distribution of precipitation within convective cells. Regions with high reflectivity values indicate areas of intense rainfall or hail within convective storms. However, the reflectivity data from MIRA-35C, working at 35 GHz (l = 8.6 mm), may present considerable attenuation when the radar beam flows through a large number of hydrometeors from the surface up to a high of approximately 4 km high (Flores-Rojas et al., 2021). By analyzing the reflectivity patterns, it becomes possible to identify episodes of deep convection around 16:30 LT, coinciding with the onset of precipitation at 16:34 LT. During this period, there is a notable presence of high reflectivity values reaching approximately 30 dBz between 1 and 4 km. Additionally, Fig. 7b illustrates the vertical velocity patterns associated with the precipitation. Positive values within the +6 m s^{-1} range indicate upward motion observed between 4 and 6 km, while negative values within the -7 m s^{-1} range signify downward motion observed between 80 and 1 km. Moreover, Fig. 7c illustrates the RMS variable which is calculated by taking the square root of the average of the squared values of the radar return signals over a specified time period. It provides a measure of the overall strength or intensity of the received signals and can be used to assess the degree of variability or turbulence within the observed region. During the period of intense convective activity the RMS variable presents values from 0.5 to 2.0 observed between 300 m and 7 km.

In relation to the remote sensing estimation, using the data of GPM-IMERG product, Fig. 8 showcases precipitation data for three precipitation events above the Mantaro valley located in the Peruvian central Andes. The region is clearly delineated, indicating the geographical area under analysis. The graphic provides a visual representation of precipitation patterns within this specific area. For example, Fig. 8a illustrates the spatial distribution of rainfall during the event that occurred on August 3, 2018 (ETM_2), at 17:00 LT. The southern region of the HYGO exhibits higher intensity rainfall, reaching approximately 15 mm h^{-1}. Similarly, in the event of September 15, 2018 (ETM_3), at 17:30 LT, Fig. 8b demonstrates that the eastern area of the HYGO experienced higher precipitation, reaching approximately 18 mm h^{-1}. Lastly, during the event on November 15, 2018, at 18:00 LT, Fig. 8c indicates that the HYGO and its surrounding region observed rainfall with intensities peaking at approximately 12 mm h^{-1}.

Based on the three mentioned criteria by using data collected from the gauge pluviometer, the MIRA-35c radar, and the GPM-IMERG product, a comprehensive analysis revealed the successful identification of a total of 21 intense precipitation events associated with convective activity on the HYGO. These findings, outlined in Table 4, encompass the period from 2018 to 2022. The total convective intense rainfall events were divided in two groups. The first group is formed by 14 events that occurred in transition months (ETM), mainly in spring and autumn seasons. The second group is formed by 07 events that occurred in rainy months (ERM) mainly in summer season. A total of 21 rainfall events were identified, all of which were associated with convective activity.

The Table 4 also provides a comprehensive overview of each event, including the respective date and the circulation type at the location of the HYGO (12.04°S, 75.32°W) at 18 UTC and at the level of 250 hPa. According to Flores-Rojas et al. (2020), the circulation types that generates intense rainfall events on the Mantaro valley can be classified into two categories: easterly or westerly, as demonstrated in Fig. 9a and b, for the dates 17 April, 2019 (ETM_8 easterly) and 28 August, 2021 (ETM_{12} westerly), respectively.

Furthermore, the Table 4 shows the timing and duration of the rainfall, as well as the hour of maximum hourly accumulated rainfall and the onset of precipitation. Additionally, we have incorporated data gathered from the MIRA-35C radar, the GPM system, and the ARPS model. As an illustration, let us consider the event that occurred on August 1, 2018, denoted as ETM_1. During this event, the wind circulation type at 250 hPa was easterly. The total duration of rainfall lasted for 4 h, commencing at 16:34 LT, with the highest hourly accumulated rainfall recorded at 17:00 LT. Throughout the event, the

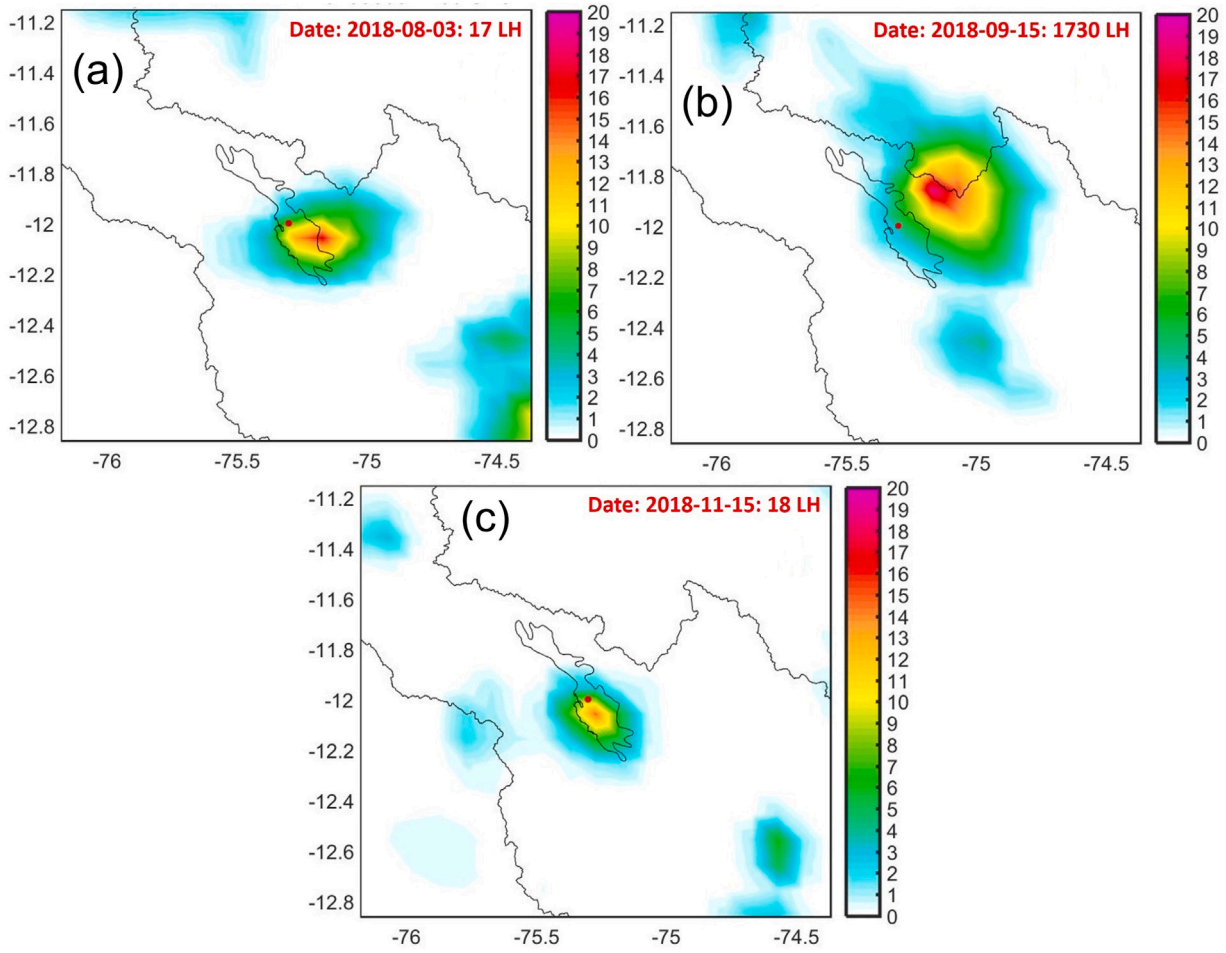

Fig. 8. Spatial distribution of precipitation rate (mm h^{1-}) around the Mantaro valley obtained from GPM-IMERG products on (a) 03 August, 2018 (ETM_2), (b) 15 September, 2018 (ETM_3) and (c) 15 November, 2018 (ETM_5).

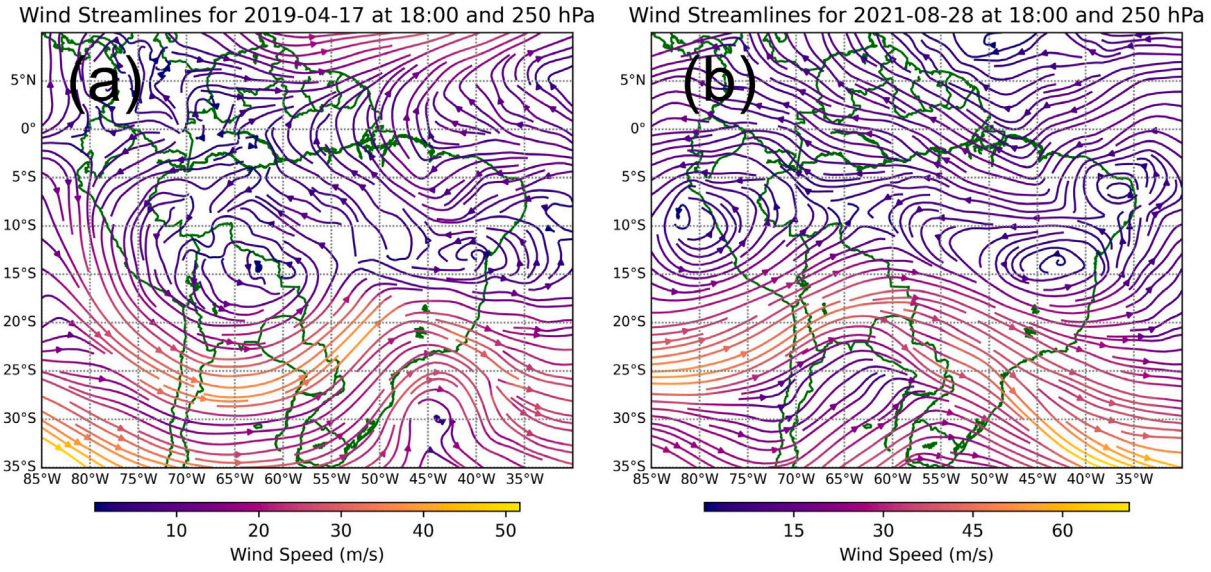

Fig. 9. Wind streamlines (m s^{-1}) from ERA5, which is the fifth generation ECMWF reanalysis for the global climate, at 18 UTC and at the level of 250 hPa for (a) 17 April, 2019 (ETM_8 easterly) and (b) 28 August, 2021 (ETM_{12} westerly).

total accumulated rainfall amounted to 10.16 mm h^{-1}, while the maximum hourly accumulated rainfall reached 5.84 mm h^{-1}. The MIRA-35c radar data revealed a maximum reflectivity of 38 dBZ and a maximum vertical velocity of +4 m s^{-1}. Furthermore, the GPM system indicated a maximum rainfall rate of 5.31 mm h^{-1}, while the ARPS model recorded no precipitation.

Table 4
The convective intense rainfall events observed above the HYGO between 2018 and 2022 were divided in two groups. The first group is formed by 14 events that occurred in transition months (ETM), mainly in spring and autumn seasons. The second group is formed by 07 events that occurred in rainy months (ERM) mainly in summer season. A total of 21 rainfall events were identified, all of which were associated with convective activity. For each event, we provided circulation types at 250 hPa and 18 UTC, timing of the rainfall, and estimation of rainfall characteristics from GPM system and radar MIRA-35c. In instances where data was unavailable, circles were used to indicate the absence of information.

Event index	Date	Wind circulation Type - 18 UTC (250 hPa)	Times of rainfall	Total rainfall ($mm\ h^{-1}$)	Maximum rainfall ($mm\ h^{-1}$)	Maximum MIRA Reflectivity (dBZ)	Maximum MIRA vertical velocity ($m\ s^{-1}$)	max GPM rainfall ($mm\ h^{-1}$)	max ARPS rainfall ($mm\ h^{-1}$)
Events in transition months (ETM)									
ETM_1	01 August 2018	Easterly	4 h (16:34 LT-17 LT)	10.16	5.84	38	+5	2.41	0.31
ETM_2	03 August 2018	Westerly	2 h (17:06 LT-17 LT)	7.87	7.62	35	+6	1.46	5.04
ETM_3	15 September 2018	Easterly	3 h (16:13 LT-16 LT)	23.62	20.32	29	+10	5.92	0.14
ETM_4	24 September 2018	Westerly	3 h (16:59 LT-17 LT)	12.45	8.64	38	+7	0.53	2.14
ETM_5	15 November 2018	Easterly	4 h (18:05 LT-18 LT)	18.03	13.46	32	+9	6.04	7.91
ETM_6	21 November 2018	Easterly	2 h (18:18 LT-18 LT)	7.62	7.11	30	+7	3.50	2.34
ETM_7	10 April 2019	Westerly	2 h (14:36 LT-14 LT)	6.86	6.60	35	+6	1.21	0.0
ETM_8	17 April 2019	Easterly	4 h (17:06 LT-17 LT)	23.37	21.59	26	+10	3.19	2.04
ETM_9	06 October 2019	Westerly	2 h (15:21 LT-15 LT)	6.22	6.20	36	+6	3.92	1.84
ETM_{10}	19 September 2020	Westerly	2 h (17:00 LT-17 LT)	11.18	10.67	29	+8	3.60	0.0
ETM_{11}	22 September 2020	Westerly	3 h (16:28 LT-17 LT)	12.95	9.65	31	+9	3.80	0.0
ETM_{12}	28 August 2021	Westerly	6 h (16:50 LT-17 LT)	34.88	23.37	26	+12	7.01	11.12
ETM_{13}	10 November 2021	Easterly	4 h (17:49 LT-18 LT)	21.33	15.49	26	+9	3.51	0.25
ETM_{14}	09 April 2022	Easterly	8 h (18:09 LT-18 LT)	24.89	8.64	30	+11	2.01	18.49
Events in rainy months (ERM)									
ERM_1	02 February 2019	Easterly	5 h (17:40 LT-18 LT)	10.92	5.08	28	+4	–	–
ERM_2	25 February 2019	Westerly	3 h (16:32 LT-16 LT)	9.40	8.64	31	+7	2.61	20.77
ERM_3	07 March 2019	Easterly	1 h (14:26 LT-14 LT)	7.37	7.37	30	+8	–	–
ERM_4	10 March 2019	Easterly	5 h (18:17 LT-21 LT)	16.00	9.40	34	+7	1.65	2.02
ERM_5	09 March 2021	Easterly	9 h (16:54 LT-17 LT)	22.30	13.21	28	+11	5.57	32.26
ERM_6	25 January 2022	Easterly	5 h (18:13 LT-18 LT)	17.78	10.67	28	+8	0.99	6.51
ERM_7	14 March 2022	Easterly	7 h (16:01 LT-17 LT)	31.24	13.97	27	+9	5.03	20.63

It is important to highlight that the peak precipitation time for all events (21) showed in Table 4 occurred between 14 and 21 LT, in accordance with the analysis of the daily and seasonal rainfall patterns at the HYGO (Fig. 4a). Moreover, it was observed that the maximum reflectivity values recorded by Mira-35 for all events were around 30 dBZ, reaching its maximum close to 40 dBZ; while the maximum vertical velocity values obtained from MIRA-35c surpassed 5 m s^{-1}, reaching its maximum around 10 m s^{-1}. It is noteworthy that the precipitation estimates obtained from GPM-IMERG consistently displayed lower magnitudes when juxtaposed with the measurements acquired from the pluviometer. Conversely, the precipitation estimates generated by the ARPS model generally demonstrated a proclivity toward higher values in contrast to the pluviometer measurements, unless instances arose where the ARPS model failed to generate any precipitation.

Furthermore, to illustrate the main characteristics of the daily cycle of some rainfall events, Fig. 10a, b, c and d, show the time series of precipitation rates above the HYGO. The data depicted in these figures were acquired from the in-situ pluviometer (represented by the red line), the Global Precipitation Measurement (GPM) dataset (depicted by the blue line), and the Advanced Regional Prediction System (ARPS) model output (indicated by the black line). The selected time periods encompass the day prior to and following the occurrence of the rainfall events on 03 August 2018 (ETM_2), 25 February 2019 (ERM_2), 09 March 2021 (ERM_5), and 14 March 2022 (ERM_7), respectively.

5.3. Simulation of turbulent energy fluxes

In this section, we present the simulation results for turbulent energy fluxes (Q_H and Q_E) obtained using the ARPS model at a spatial resolution of 0.5 km, focusing on all extreme rainfall events listed in Table 4. As an illustrative example, Fig. 11a and b depict the spatial distribution of Q_H and Q_E over the Mantaro valley during the event on November 15, 2018 (ETM_5) at 14:50 LT (19:50 UTC). Notably, at this specific time, we observed high values of Q_H and Q_E in the proximity of the HYGO, peaking at approximately 250 W m^{-2} and 500 W m^{-2}, respectively. These turbulent energy fluxes originate primarily from the

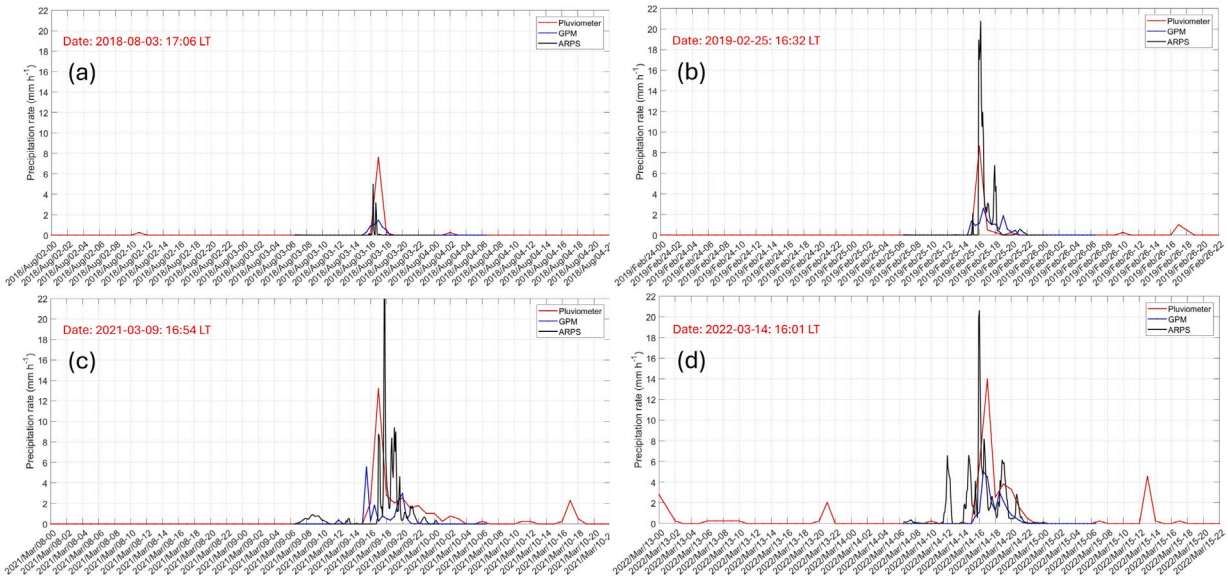

Fig. 10. Time series of precipitation rate (mm h^{-1}) obtained from in situ gauge pluviometer (red line) GPM-IMERG product (blue line) and ARPS model (black line) for (a) 03 August, 2018 (ETM_2), (b) 25 February, 2019 (ERM_2), (c) 09 March, 2021 (ERM_5) and (d) 14 March, 2022 (ERM_7).

north-western region of the HYGO. It is important to emphasize that these peak values of Q_H and Q_E are reached approximately three hours before the onset of the intense rainfall event. This temporal pattern is clearly depicted in Fig. 11c, which presents the daily variation of Q_H and Q_E spanning from 07:00 LT to 23:55 LT during the November 15, 2018 (ETM_5) event. Notably, the onset of the intense rainfall event, occurring around 17:50 LT, is distinctly marked by a black vertical line on the graph.

Fig. 12a and b provide a comparison between Q_H and Q_E estimations using both the bulk aerodynamic method and the ARPS model for all intense rainfall events listed in Table 4 at a 1 min time resolution. In both plots, the red line represents the regression line, while the blue line corresponds to the 45-degree line. For Q_H, the analysis yields an R^2 value of 0.56 with a linear regression equation: $Y = 18.27 + 0.48 \times X$. Notably, for Q_H values up to 450 W m^{-2}, the ARPS model consistently underestimates the bulk aerodynamic method estimates, as indicated by the slope of the linear regression (0.48). Conversely, for Q_E, the R^2 value is 0.24, and the linear regression equation is $Y = 48.0 + 0.45 \times X$. Interestingly, in contrast to Q_H, the ARPS model tends to overestimate the bulk aerodynamic method estimations for low Q_E values, but exhibits a behavior similar to Q_H for high Q_E values, as reflected in the slope of the linear regression (0.45).

To illustrate these characteristics, Fig. 13a depicts the daily variation of Q_E, as estimated by both the bulk aerodynamic method and the ARPS model on August 01, 2018 (ETM_1). During this event, an observed phase shift of approximately four hours is evident, with the ARPS model signal lagging behind, eventually reaching values close to 100 W m^{-2} around noon. Furthermore, Fig. 13b presents the daily variation of Q_E for November 21, 2018 (ETM_6). During this particular event, a notably higher degree of resemblance exists between the Q_E values estimated by the bulk aerodynamic method and those predicted by the ARPS model. Additionally, the phase shift between these signals is reduced, with the ARPS model consistently overestimating Q_E, reaching values of approximately 300 W m^{-2}. Moving on, Fig. 13c and d illustrate the daily profile of Q_H for March 10, 2019 (ERM_4) and September 22, 2020 (ETM_{11}), respectively. For event ERM_4, the ARPS model significantly underestimates Q_H values, particularly around noon, with differences of up to 150 W m^{-2} compared to estimates obtained using the bulk aerodynamic method. Conversely, during event ETM_{11}, there is a greater degree of concordance between the Q_H values estimated by the bulk aerodynamic method and those predicted by the ARPS model, with peak values nearing 250 W m^{-2} around noon.

5.4. Monthly and daily variations of SEB components at HYGO

In this section we presented a detailed description of monthly and daily variations of the mean SEB components on the HYGO between May 2018 and December 2022. The mean monthly and daily variations for the net irradiance flux (Q^*) are shown in Fig. 14a. The fluctuations in the Q^*, as observed throughout the year and at different hours of the day, serve to illustrate the dynamic shifts in the equilibrium between incoming and outgoing short-wave and long-wave irradiance. During the austral summer (December-February), the Q^* peaks at 640–720 W m^{-2} around 11:00 LT, whereas it is lowest, ranging from 0–80 W m^{-2}, at night, notably in February and March. Transitional seasons of autumn (March-May) and spring (September-November) mark intermediate Q^* values: maximums range between 560–640 W m^{-2} around 11:00-12:00 LT, while minimums span −80 to 0 W m^{-2} at night. The winter months (June-August) see the lowest Q^* values, with peak readings of 480–560 W m^{-2} during 11:00-12:00 LT and trough values of −80 to 0 W m^{-2} at night. Fig. 14a depicts seasonal sunshine duration variation, showcasing distinct yearly patterns reflecting solar radiation changes at the HYGO. Longer daylight spans from 05:30-17:30 LT (approximately 12 h) in summer, whereas winter exhibits the shortest sunshine duration, from 06:00-17:00 LT (approximately 11 h).

In addition, the mean monthly and daily variations of the ground heat flux (Q_G) are described, as depicted in Fig. 14b. During the summer months, the Q_G exhibits near-zero values during the night hours, specifically from 22:00 to 05:30 LT. Subsequently, from 05:30 to 11:00 LT, positive values are observed, reaching maximums ranging from 150 to 250 W m^{-2}, particularly in December. Following this period, from 11:30 to 21:45 LT, the Q_G becomes negative, with minimums ranging from −50 to −250 W m^{-2}, predominantly in December. During the autumn and winter months, the behavior of the Q_G demonstrates a remarkable symmetry. Positive maximum values, peaking around 200 W m^{-2}, are recorded between 05:30 and 11:00 LT, while negative minimum values, approaching -200 W m^{-2}, are observed from 11:30 to 19:00 LT. For the remaining hours, the Q_G remains close to zero. Notably, during the spring months, particularly in October, the Q_G displays positive values for a significant portion of the day, with the highest maximums reaching approximately 350 W m^{-2} occurring around 09:00 LT. Conversely, in November and December, negative values dominate, with the highest minimums close to −250 W m^{-2} occurring around 14:00 LT.

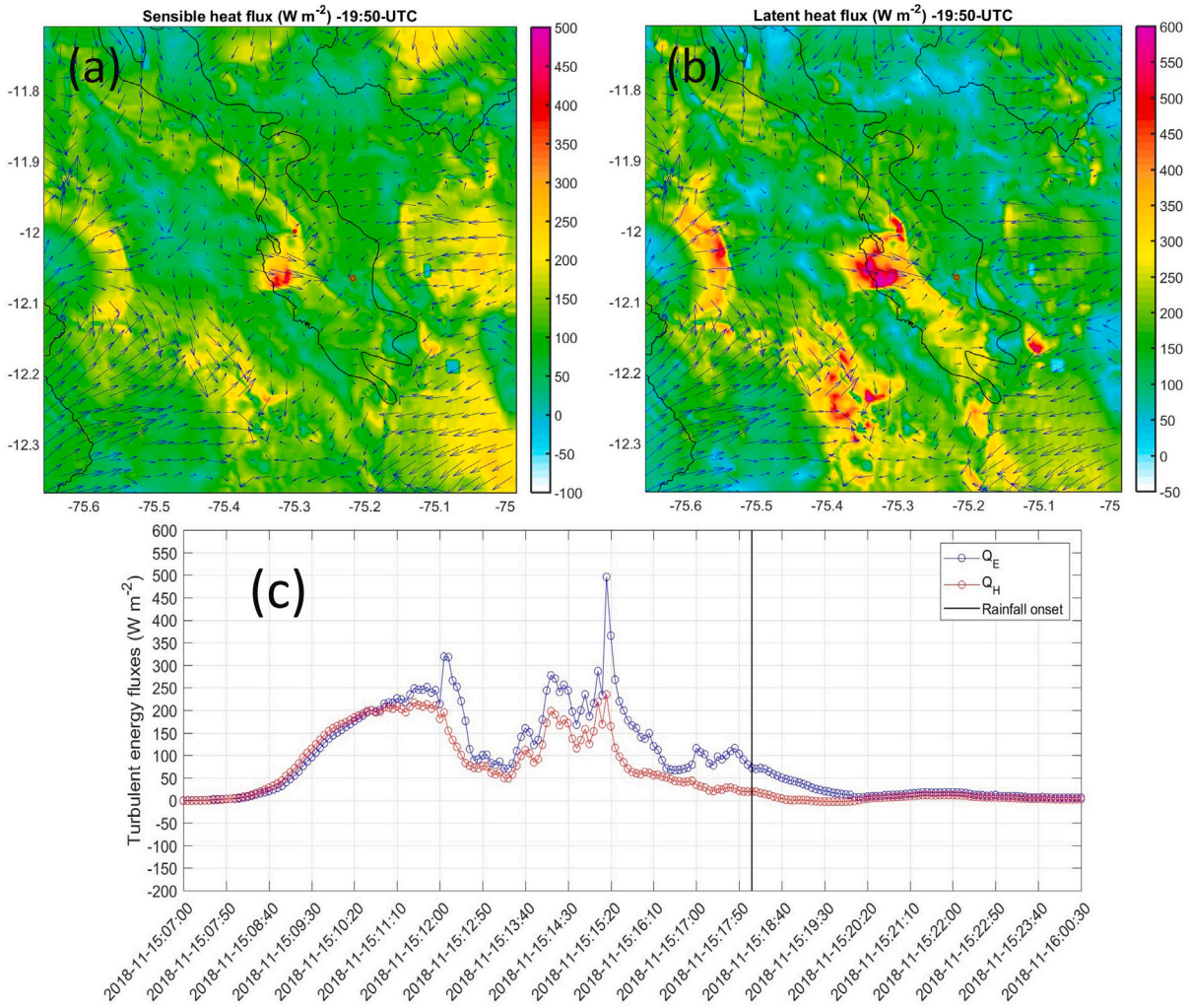

Fig. 11. Spatial distribution of (a) Q_H (W m^{-2}) and (b) Q_E (W m^{-2}) around the Mantaro valley during the event on 15 November 2018 (ETM_5). The red point indicates the location of the HYGO. (c) Daily variations of Q_H and Q_E (W m^{-2}) between 07 LT and 00 LT during the event on 15 November 2018 (ETM_5). All data in the graphics were obtained with the ARPS model.

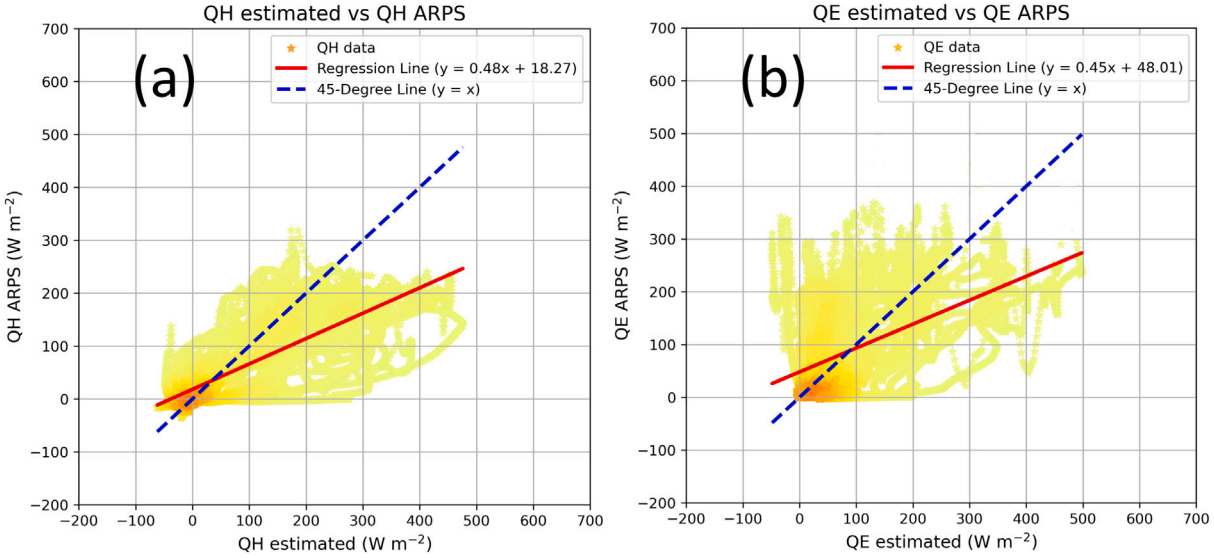

Fig. 12. The scatter plot illustrates the comparison between the measured (a) Q_H and (b) Q_E (W m^{-2}), as determined by the aerodynamic method, and the corresponding simulations of Q_H and Q_E produced by the ARPS model at a 1 min temporal resolution. The data points on the plot correspond to all events listed in Table 4.

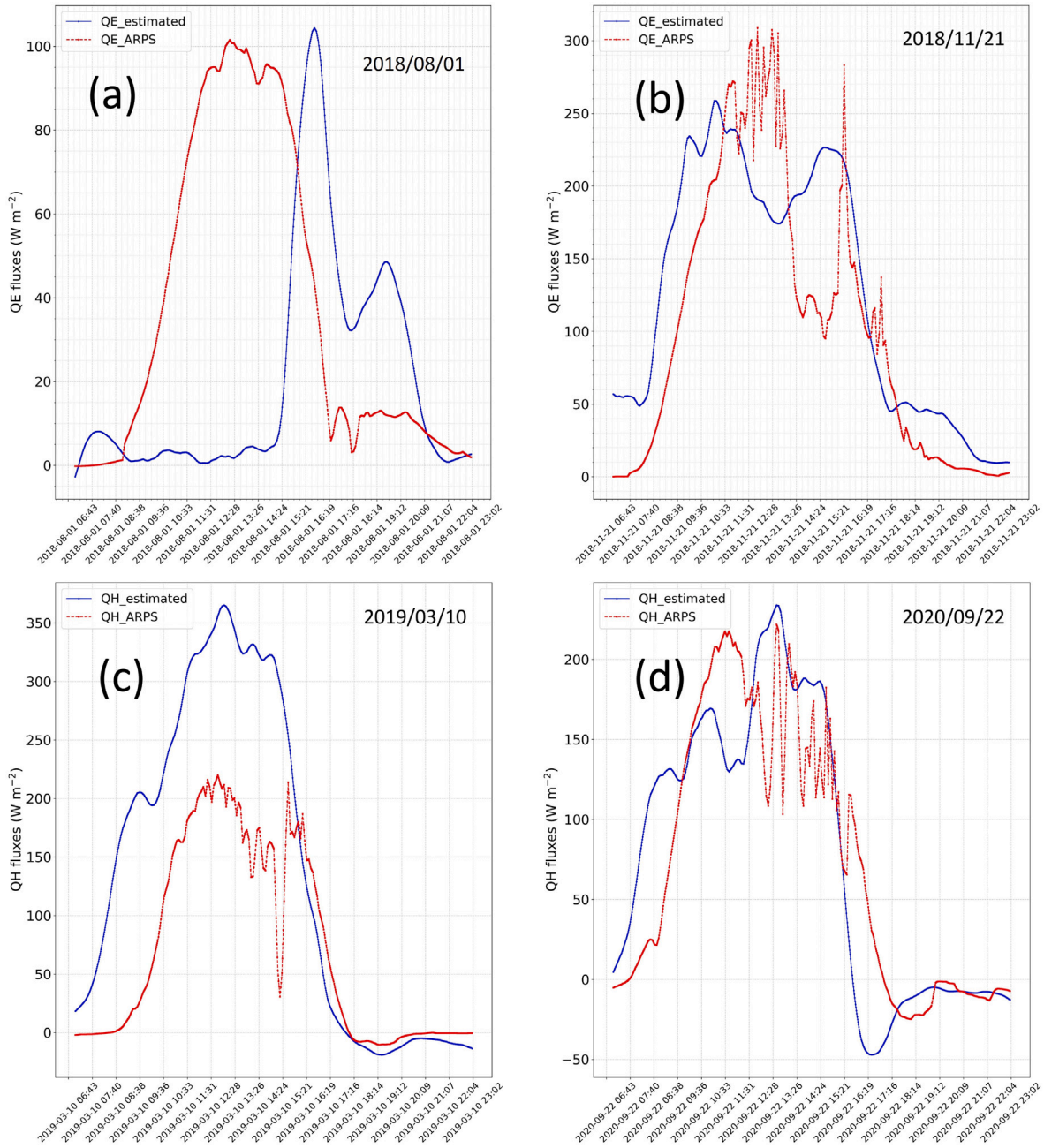

Fig. 13. Daily variation of Q_E (W m^{-2}) measured by the bulk aerodynamic method and estimated by the ARPS model for (a) 2018-08-01 (ETM_1) and (b) 2018-11-21 (ETM_6). Daily variation of Q_H (W m^{-2}) measured by the aerodynamic method and estimated by the ARPS model for (c) 2019-03-10 (ERM_4) and (d) 2020-09-22 (ETM_{11}).

In addition, Fig. 14c shows the mean monthly and daily variations of the latent heat flux (Q_E). During the summer months, the latent heat flux exhibits notable peaks, ranging between 200 and 225 W m^{-2}, occurring from 11:00 to 14:00 LT. However, the highest values are observed in March, with values approaching 250 W m^{-2} between 12:00 and 13:00 LT. Subsequently, as the autumn months progress, the flux diminishes gradually, eventually reaching lower values during winter, ranging from 25 to 50 W m^{-2} between 11:00 and 13:00 LT. In contrast, the Q_E experiences an upward trend during the spring months, gradually rising from 50 to 125 W m^{-2} around midday. During nocturnal hours, the Q_E reaches its lowest values during the winter months, with values close to −25 W m^{-2} during early morning hours.

Besides, Fig. 14d shows the mean monthly and daily variations of the sensible heat flux (Q_H). The highest values, ranging from 240 to 270 W m^{-2}, are observed during the spring months, specifically from 11:00 to 13:00 LT. Throughout the winter months, intermediate values between 180 and 240 W m^{-2} are observed within the same time range. In the summer months, the Q_H reaches its maximum around 12:00 LT, with values close to 180 W m^{-2}. Conversely, during the autumn months, the Q_H exhibits the lowest values, ranging between 150 and 180 W m^{-2}. During the nocturnal hours, the Q_H remains consistently between −30 and 0 W m^{-2} across all months.

Moreover, the mean monthly and daily variations of the momentum flux (τ) are illustrated in Fig. 14e. The highest values, ranging from 0.16 to 0.22 m^2 s^{-2}, are predominantly observed from 15:00 to 17:00 LT, encompassing the latter part of the winter months, the spring months, and December. Intermediate values of approximately 0.12 m^2 s^{-2} are evident during the early summer, specifically from 14:00 to 17:00 LT. Conversely, the lowest values of the τ, ranging between 0.10 and 0.12 m^2 s^{-2}, are observed during the autumn months within the same

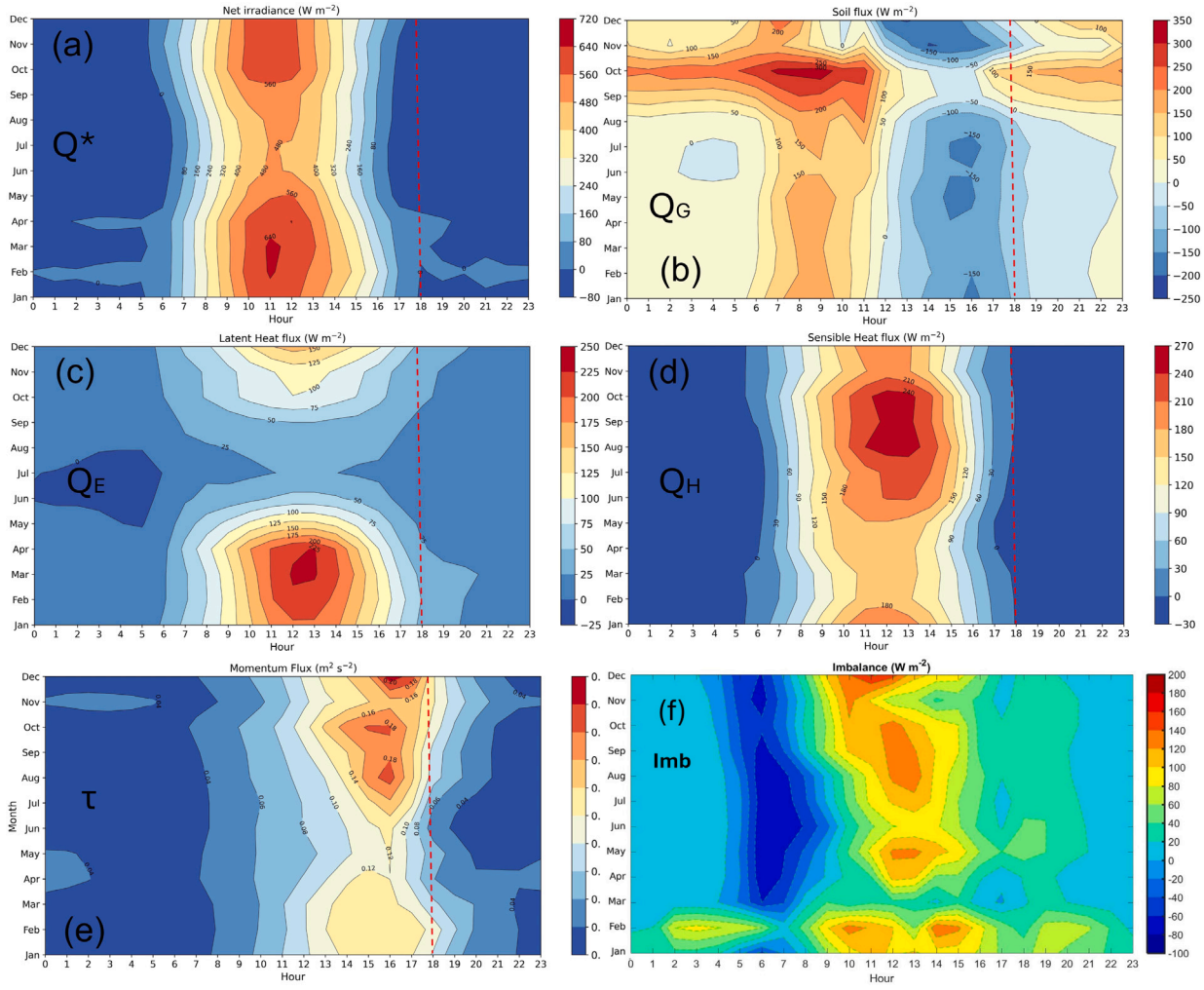

Fig. 14. Monthly and daily variations of the mean SEB components on the HYGO between May 2018 and December 2022. The components shown are: (a) Net irradiance (Q^*), (b) Soil heat flux (Q_G), (c) Latent heat flux (Q_E), (d) Sensible heat flux (Q_H), (d) Momentum flux (τ) and (e) Imbalance term, (Imb). All components are measures in W m^{-2} except for τ which is m^2 s^{-2}. The behavior of the SEB components during the maximum hourly mean precipitation at the HYGO at 18 LT, is illustrated by the vertical dotted lines.

time frame of 15:00 to 17:00 LT. Throughout the nocturnal hours, a consistent range of 0.02 to 0.04 m^2 s^{-2} characterizes the τ across all months.

On the other hand, it should be noted that the bulk aerodynamic method is an approximate method, and a better estimation of turbulent energy fluxes (Q_H and Q_E) is by using an eddy covariance equipment, as verified by several studies. Despite this, as the first approximation, the imbalance term in Eq. (8) was estimated by using the turbulent energy-balance fluxes using the aerodynamic method.

$$Q^* - Q_H - Q_E - Q_G = -TT - A + S + B + O_t = Imb \quad (8)$$

The imbalance term (Eq. (1)) considers several terms. These terms include transient conditions such as morning or evening transitions (TT), advection of heat due to local heterogeneities (A), storage in the elements of the volume (S), biological processes (B) and instrumental errors (O_t). These terms can be grouped in the imbalance (Imb). As shown in Fig. 14f, for all months, after sunrise the imbalance became negative with values between −50 W m^{-2} and -100 W m^{-2}. Next, the imbalance increased up to reach positive values with the minimum close to +80 W m^{-2} and the maximum close to +200 W m^{-2}. The most negative imbalance values were observed between 05 and 09 LT, mainly during fall and winter months and the most positive imbalance values were observed 11 and 15 LT during spring and summer months.

The presence of these imbalance values can be explained due to the instrumental errors, the errors associated with the methods to estimate turbulent energy fluxes and due to the long-lasting terrain heterogeneities on the hectometer (100 m) scale. Moreover, the surface on which the sensors measured the meteorological variables is a natural vegetation canopy that it is not irrigated at any time of the year. In contrast, surrounding this natural canopy, there are several cultivated fields and small woods that are frequently irrigated. This contrast can explain a significant part of the imbalance, especially after sunrise and at noon, as the temperature gradients may generate motions that last longer than the averaging time of the turbulent fluxes. Moreover, the mountain–valley circulation can also contribute to the enhance of the advective process of energy. However, more conclusive evidence is needed to verify these hypotheses by performing experiments specifically designed to estimate the sign of the advection term.

5.5. Daily variations of Q_G: Underlying mechanisms and environmental influences

Understanding the dynamics of Q_G is essential for accurate surface energy modeling and local climate predictions. The afternoon recovery of soil heat flux, influenced by shifts in evapotranspiration, cloud variability, and soil thermal properties, directly affects surface temperatures. In Fig. 14b, during spring months, it is possible to observe a decrease in Q_G after noon followed by a subsequent increase to positive values in the afternoon, around 17 LT. This behavior, while unusual, can be explained by several environmental and physical processes. Here

is a detailed explanation of the possible causes, some of them described in Flores-Rojas et al. (2019a):

1. During spring months, after solar noon, the surface energy balance undergoes changes due to declining solar radiation. However, soil heat flux is not only influenced by incoming solar radiation but also by how energy is redistributed between the other components of the surface energy balance (Q^*, Q_H, and Q_E). In the afternoon, evapotranspiration (or evaporation) can increase significantly due to higher vapor pressure deficits and atmospheric mixing. This consumes a large fraction of the available energy at the surface. As more energy is directed toward Q_E, the surface cools slightly, leading to a reduction in downward heat flux into the soil. Once latent heat flux reduces (e.g., later in the afternoon when humidity rises or wind subsides), more energy becomes available for soil heat flux, which can cause positive flux values to reappear.
2. After solar noon, if the surface cools momentarily due to cloud cover or increased wind-driven convective cooling, Q_G may decrease or even reverse. If the surface heats again later in the afternoon (e.g., due to clearing skies or reduced wind), Q_G can increase and become positive again. Variations in cloud cover or atmospheric conditions in the afternoon can cause temporary reductions or increases in surface heat input, leading to complex behavior in Q_G. Passing clouds reduce incoming solar radiation, cooling the surface and causing a decrease in Q_G after noon. Once the clouds clear, surface temperatures can quickly rise, reestablishing a positive Q_G. This phenomenon is particularly pronounced in areas with convective cloud development like the Mantaro valley, where cloud cover fluctuates rapidly during the afternoon. After clouds dissipate in the afternoon, the net longwave radiation at the surface may temporarily exceed losses, causing additional surface warming and increasing Q_G.
3. The thermal properties of the soil, such as thermal conductivity and heat capacity, play a crucial role in determining how heat is stored and transferred. After noon, heat stored in the surface layer can continue to transfer downward due to thermal gradients, leading to an increase of Q_G later in the afternoon. Soils with high heat capacity store significant amounts of heat during the day. If the surface is warmer than the subsurface layers in the afternoon, stored heat may flow downward, creating positive Q_G values. As the soil adjusts to changing surface temperatures, temporary decreases or increases in Q_G may occur.
4. Finally, as in the nighttime case, horizontal advection of warm air can influence surface temperatures and Q_G even during the afternoon. Warm air transported into the region by wind can create temporary surface heating, which increases the temperature gradient and drives positive Q_G downward into the soil. Afternoon advection often occurs in regions with significant terrain effects, such as the Mantaro valley where exist mountain valley circulations.

5.6. Daily variation of SEB components during intense rainfall events at HYGO

The daily variation of surface energy balance (SEB) components (Q^* Q_G, Q_E, Q_H, and τ), was examined in relation to convective rainfall events at the HYGO location. A comparative analysis was conducted between the SEB components before, during and after the occurrence of convective rainfall events and the average SEB components observed for 15 preceding days devoid of any rainfall conditions. This analysis was performed for the total 21 identified intense rainfall events at HYGO which are shown in Table 5 for Q^* and Q_G and in Table 6 for Q_E, Q_H and τ. It is important to highlight that 14 of 21 events (66.6%) occurred during transition months, while 07 events (33.33%) occurred during rainy months. For transition months, the frequency of intense precipitation varies between 7.7% and 11.3%, while for rainy months varies between 7.8% and 9.9% (Fig. 5a,b).

5.6.1. Net irradiance (Q^*)

During intense precipitation events, the peak intensity of Q^* preceded the highest Q^* intensity recorded in the preceding 15 days without precipitation in 11 out of 18 events (61.1%). In contrast, for 5 events (27.8%), the peak intensity coincided with the maximum observed in the dry period, while in 2 events (11.1%), it occurred after the dry-period maximum. Furthermore, a significant decrease in Q^* values was observed immediately following the peak intensity, primarily due to increased cloud cover compared to the conditions of the preceding 15 days without precipitation.

This pattern is evident in Fig. 15a, which illustrates the winter event on August 1, 2018 (ETM_1), and in Fig. 16a, which depicts the autumn event on March 14, 2022 (ERM_7). In Fig. 15a, the evolution of Q^* during the convective rainfall event ETM_1 (winter season) is compared to its behavior in the preceding 15 days without precipitation. The onset of precipitation at 16:34 LT is marked by a dotted vertical line. During the event, mean Q^* values exhibit a sharp decline between 10:00 and 15:00 LT, reaching a maximum of approximately 459.2 ± 128.8 W m^{-2} at 10:00 LT. In contrast, during the 15-day dry period before the event, mean Q^* values peaked at approximately 475 ± 81 W m^{-2} at 11:00 LT. This peak closely aligns with the climatological mean for August at this time of day, as shown in Fig. 14a.

A similar behavior is observed for the convective rainfall event ERM_7 (autumn season), as illustrated in Fig. 16a. During this event, a pronounced decrease in mean Q^* values occurs between 10:00 and 15:00 LT, with a peak of approximately 722.1 ± 323.5 W mm^{-2} at 10:00 LT. In contrast, during the preceding 15 days, the maximum Q^* value reached 851 ± 257 W m^{-2} at 11:00 LT, exceeding the climatological mean for March at this time (640 W m^{-2}).

5.6.2. Soil heat flux (Q_G)

On the other hand, during intense precipitation events, the minimum peak intensity of Q_G preceded the lowest Q_G intensity recorded in the preceding 15 days without precipitation in 16 of 20 events (80%). In contrast, for 3 events (15%), the peak intensity coincided with the minimum observed in the dry period, while in 1 events (5.0%), it occurred after the dry-period minimum (Table 5). This pattern is clearly illustrated in Figs. 15b and 16b. Notably, during the most intense precipitation events, the minimum Q_G intensity was lower than the levels observed during the preceding 15 precipitation-free days. This trend is clearly illustrated in Figs. 15b and 16b.

Fig. 15b shows the comparison of Q_G mentioned above for the convective rainfall event ETM_1 (winter season). The onset of precipitation at 16:34 LT is indicated by a dotted vertical line. The mean values of Q_G for the 15 days leading up to the event demonstrate maximums close to 193 ± 52 W m^{-2} at 09 LT, and minimums close to −194 ± 33 W m^{-2} at 17 LT. These values closely correspond to the mean values of Q_G observed throughout the entire analysis period in August, as illustrated in Fig. 14b. In contrast, during the event, the mean values of Q_G present an oscillatory behavior from 12 to 15 LT, reaching its maximum at 13 LT with values close to 19 ± 153 W m^{-2} and its minimum at 15 LT with values close to −283 ± 15 W m^{-2}. This behavior is similar to the observed during the convective rainfall event ERM_7 (autumn season), as shown in Fig. 16b. However, the maximum Q_G for the 15 preceding days of this event reaches values close to 137 ± 70 W m^{-2} at 08 LT, slightly lower than the mean values of Q_G during March (Fig. 14b). Similarly to the previous event, an oscillatory behavior of Q_G is observed from 12 to 15 LT during the event, reaching its maximum at 13 LT with values close to 82 ± 149 W m^{-2} and its minimum at 15 LT with values close to −150 ± 117 W m^{-2}.

5.6.3. Latent heat flux (Q_E)

In addition, during intense precipitation events, the maximum peak intensity of Q_E occurred after the dry-period maximum in 12 of 21 events (57.14%). In contrast, for 6 events (28.57%), the maximum peak intensity coincided with the maximum observed in the dry-period,

Table 5
Surface energy balance (SEB) components Q^* and Q_G were analyzed during intense rainfall events identified at the HYGO, as well as for 15 preceding days without rainfall. The analysis focused on two groups: the first comprised 14 events during transition months (spring and autumn), while the second consisted of 07 events during rainy months (summer). In total, 21 convective activity-associated rainfall events were identified.

Event	Onset	Q^* (W m^{-2})				Q_G (W m^{-2})			
	rainfall (LT)	Day event		15 days before		Day event		15 days before	
		Hour Max	Value Max	Hour Max	Value Max	Hour Min	Value Min	Hour Min	Value Min
Events in transition months (ETM)									
ETM_1	16:34 LT	10 LT	459.2 ± 128.8	11 LT	475.8 ± 77.9	15 LT	−282.9 ± 15.1	17 LT	−194.4 ± 33.1
ETM_2	17:06 LT	11 LT	555.0 ± 157.0	11 LT	483.7 ± 79.5	13 LT	−224.6 ± 18.5	17 LT	−198.5 ± 33.7
ETM_3	16:13 LT	10 LT	513.1 ± 112.5	11 LT	567.3 ± 69.1	15 LT	−232.4 ± 30.4	17 LT	−218.2 ± 29.8
ETM_4	16:59 LT	09 LT	497.7 ± 21.4	10 LT	470.6 ± 95.2	16 LT	−198.7 ± 59.8	17 LT	−199.2 ± 34.2
ETM_5	18:05 LT	–	–	10 LT	446.5 ± 51.3	14 LT	−172.1 ± 124.8	17 LT	−172.2 ± 43.9
ETM_6	18:18 LT	–	–	10 LT	430.0 ± 53.9	13 LT	−216.2 ± 44.3	16 LT	−192.2 ± 60.0
ETM_7	14:36 LT	12 LT	737.1 ± 7.88	12 LT	585.8 ± 55.1	14 LT	−244.7 ± 1.28	16 LT	−117.8 ± 42.5
ETM_8	17:06 LT	12 LT	625.9 ± 187.4	12 LT	626.2 ± 71.7	13 LT	−140.9 ± 157.5	16 LT	−116.4 ± 44.1
ETM_9	15:21 LT	10 LT	601.5 ± 112.3	11 LT	468.4 ± 130.5	15 LT	−136.4 ± 56.7	16 LT	−185.1 ± 53.1
ETM_{10}	17:00 LT	11 LT	659.1 ± 119.8	14 LT	484.9 ± 83.6	14 LT	−217.9 ± 85.9	16 LT	−147.3 ± 57.8
ETM_{11}	16:28 LT	11 LT	696.2 ± 21.1	11 LT	717.0 ± 5.6	16 LT	−287.6 ± 0.7	16 LT	−135.9 ± 62.1
ETM_{12}	16:50 LT	11 LT	637.7 ± 9.2	12 LT	597.0 ± 48.9	–	–	16 LT	−150.7 ± 39.8
ETM_{13}	17:49 LT	10 LT	492.3 ± 29.4	12 LT	634.1 ± 118.2	16 LT	−220.8 ± 23.7	16 LT	−143.6 ± 35.3
ETM_{14}	18:09 LT	13 LT	793.5 ± 95.8	11 LT	580.7 ± 107.3	14 LT	−216.1 ± 74.9	16 LT	−136.8 ± 47.6
Events in rainy months (ERM)									
ERM_1	17:40 LT	11 LT	802.6 ± 105.8	–	–	17 LT	−227.4 ± 54.4	17 LT	−213.4 ± 48.6
ERM_2	16:32 LT	12 LT	496.4 ± 102.4	11 LT	545.8 ± 125.3	12 LT	−48.0 ± 215.18	17 LT	−148.0 ± 39.1
ERM_3	14.26 LT	11 LT	830.5 ± 132.1	12 LT	561.5 ± 182.6	13 LT	−165.2 ± 53.7	17 LT	−162.3 ± 49.9
ERM_4	18:17 LT	12 LT	784.1 ± 388.7	12 LT	618.4 ± 194.5	12 LT	−196.6 ± 0.20	17 LT	−163.1 ± 49.1
ERM_5	16:54 LT	12 LT	688.0 ± 209.0	13 LT	533.5 ± 179.6	16 LT	−175.5 ± 25.1	17 LT	−135.6 ± 32.4
ERM_6	18:13 LT	11 LT	854.9 ± 154.5	12 LT	610.1 ± 126.3	17 LT	−155.3 ± 43.9	16 LT	−136.2 ± 43.9
ERM_7	16:01 LT	10 LT	722.1 ± 323.5	11 LT	851.3 ± 257.7	15 LT	−149.8 ± 117.9	16 LT	−122.3 ± 50.4

Table 6
Surface energy balance (SEB) components Q_E, Q_H and τ during the intense rainfall events identified at the HYGO and for 15 preceding days devoid of any rainfall conditions. The analysis focused on two groups: the first comprised 14 events during transition months (spring and autumn), while the second consisted of 7 events during rainy months (summer). In total, 21 convective activity-associated rainfall events were identified.

Event	Onset	Q_E				Q_H				τ			
	rainfall (LT)	Day event		15 days before		Day event		15 days before		Day event		15 days before	
		Hour Max	Value Max	Hour Max	Value Max	Hour Min	Value Min	Hour Min	Value Min	Hour Min	Value Min	Hour Min	Value Min
Events in transition months (ETM)													
ETM_1	16:34 LT	16 LT	95.0 ± 8.9	12 LT	20.0 ± 2.2	13 LT	299.9 ± 7.8	14 LT	289.9 ± 20.5	16 LT	0.64 ± 0.09	16 LT	0.20 ± 0.02
ETM_2	17:06 LT	13 LT	62.1 ± 4.3	12 LT	25.9 ± 2.8	11 LT	304.9 ± 20.6	12 LT	275.6 ± 22.5	17 LT	0.16 ± 0.02	16 LT	0.19 ± 0.02
ETM_3	16:13 LT	16 LT	35.2 ± 3.3	13 LT	12.2 ± 1.5	10 LT	445.0 ± 28.4	13 LT	286.6 ± 14.5	15 LT	0.31 ± 0.06	16 LT	0.17 ± 0.02
ETM_4	16:59 LT	13 LT	122.9 ± 4.4	13 LT	56.8 ± 4.8	11 LT	430.5 ± 9.3	12 LT	310.0 ± 23.5	16 LT	0.23 ± 0.03	15 LT	0.18 ± 0.01
ETM_5	18:05 LT	13 LT	236.3 ± 12.5	12 LT	221.8 ± 9.2	13 LT	365.7 ± 22.5	12 LT	241.2 ± 9.5	13 LT	0.30 ± 0.05	18 LT	0.12 ± 0.02
ETM_6	18:18 LT	11 LT	245.5 ± 8.5	12 LT	210.2 ± 12.1	11 LT	240.2 ± 11.7	12 LT	228.4 ± 9.7	15 LT	0.15 ± 0.01	17 LT	0.17 ± 0.04
ETM_7	14:36 LT	12 LT	357.8 ± 21.2	13 LT	296.5 ± 9.2	10 LT	319.6 ± 12.5	11 LT	222.6 ± 13.6	21 LT	0.23 ± 0.04	15 LT	0.13 ± 0.02
ETM_8	17:06 LT	12 LT	347.8 ± 10.8	12 LT	286.2 ± 15.9	12 LT	337.6 ± 3.4	10 LT	243.5 ± 10.5	13 LT	0.18 ± 0.02	14 LT	0.11 ± 0.02
ETM_9	15:21 LT	07 LT	24.2 ± 3.3	07 LT	18.0 ± 3.7	13 LT	441.6 ± 14.3	12 LT	338.3 ± 22.9	15 LT	0.24 ± 0.01	16 LT	0.24 ± 0.03
ETM_{10}	17:00 LT	18 LT	58.5 ± 9.7	16 LT	26.9 ± 3.1	11 LT	210.7 ± 18.8	13 LT	165.3 ± 12.3	18 LT	0.23 ± 0.05	16 LT	0.14 ± 0.01
ETM_{11}	16:28 LT	17 LT	75.7 ± 8.0	15 LT	30.1 ± 3.7	13 LT	223.4 ± 7.8	13 LT	172.3 ± 12.5	15 LT	0.22 ± 0.03	16 LT	0.13 ± 0.01
ETM_{12}	16:50 LT	08 LT	86.6 ± 1.4	12 LT	39.0 ± 2.6	12 LT	183.9 ± 9.7	13 LT	231.2 ± 13.2	16 LT	0.15 ± 0.02	16 LT	0.17 ± 0.02
ETM_{13}	17:49 LT	13 LT	89.4 ± 3.6	12 LT	124.5 ± 6.6	12 LT	282.1 ± 8.9	12 LT	267.9 ± 14.1	17 LT	0.11 ± 0.01	16 LT	0.18 ± 0.02
ETM_{14}	18:09 LT	13 LT	389.5 ± 16.7	13 LT	239.3 ± 11.9	13 LT	200.4 ± 10.6	10 LT	154.3 ± 9.9	20 LT	0.24 ± 0.02	13 LT	0.13 ± 0.02
Events in rainy months (ERM)													
ERM_1	17.40 LT	13 LT	285.6 ± 24.0	12 LT	170.0 ± 7.9	14 LT	195.9 ± 25.3	12 LT	182.9 ± 7.3	17 LT	0.23 ± 0.02	12 LT	0.07 ± 0.001
ERM_2	16:32 LT	13 LT	365.7 ± 9.5	12 LT	333.0 ± 15.9	13 LT	242.5 ± 15.7	11 LT	230.4 ± 16.4	15 LT	0.32 ± 0.03	16 LT	0.21 ± 0.02
ERM_3	14:26 LT	12 LT	385.8 ± 11.7	12 LT	310.5 ± 15.0	12 LT	274.5 ± 9.1	12 LT	215.2 ± 14.7	14 LT	0.27 ± 0.02	16 LT	0.20 ± 0.03
ERM_4	18:17 LT	13 LT	467.8 ± 18.0	12 LT	302.8 ± 14.9	12 LT	343.4 ± 13.4	12 LT	210.8 ± 15.4	13 LT	0.15 ± 0.01	16 LT	0.22 ± 0.03
ERM_5	16:54 LT	15 LT	179.8 ± 7.7	13 LT	158.8 ± 10.4	12 LT	276.7 ± 11.7	13 LT	228.3 ± 18.3	18 LT	0.30 ± 0.05	14 LT	0.15 ± 0.01
ERM_6	18:13 LT	13 LT	247.8 ± 10.2	13 LT	186.2 ± 11.7	13 LT	170.2 ± 5.7	12 LT	209.7 ± 16.0	18 LT	0.16 ± 0.02	17 LT	0.15 ± 0.02
ERM_7	16:01 LT	14 LT	211.9 ± 9.6	11 LT	209.9 ± 14.3	10 LT	130.8 ± 6.9	11 LT	138.1 ± 10.2	16 LT	0.20 ± 0.02	14 LT	0.12 ± 0.02

while in 3 events (14.28%) preceded the maximum peak intensity of Q_E. Furthermore, it was also observed that the maximum Q_E intensity surpassed that of the 15 previous days without precipitation as seen in the Figs. 15c and 16c.

Fig. 15c shows the comparison mentioned above of Q_E for the convective rainfall event ETM_1 on 01 August, 2018 (winter season). Precipitation onset at 16:34 LT is marked by a dotted vertical line. Mean Q_E values for the 15 days preceding the event peaked at 12 LT, (approximately 20 ± 2 W m^{-2}). This value is slightly lower than the mean Q_E values at this time in August (Fig. 14c). During the event, Q_E begins to increase significantly from 14 LT reaching its maximum value close to 95 ± 9 at 16 LT. Conversely, for the convective rainfall event ERM_7 (autumn season), shown in Fig. 16c, the maximum Q_E for the 15 preceding days of this event reached maximum values close

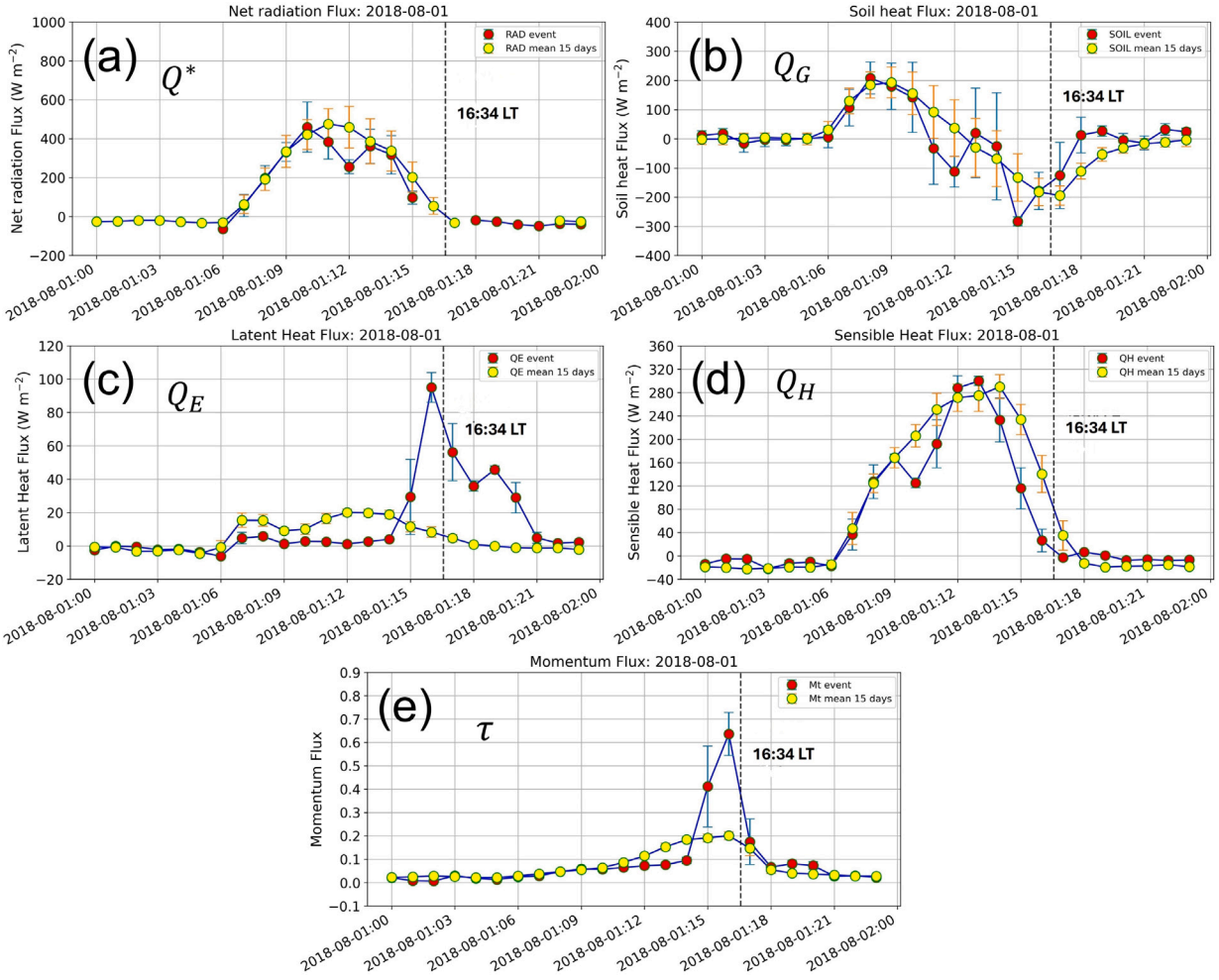

Fig. 15. Daily variation of the SEB components during the intense rainfall event at 01 August, 2018 (ETM_1) and for the previous 15 days without any rainfall conditions. (a) Net irradiance (Q^*), (b) Soil heat flux (Q_G), (c) Latent heat flux (Q_E), (d) Sensible heat flux (Q_H) and (e) Momentum flux (τ). All components are measures in W m^{-2} except for τ which is m^2 s^{-2}. The initial time of the intense rainfall event at 16:34 LT is denoted by the dotted vertical lines.

to 210 ± 14 W m^{-2} at 11 LT, slightly lower than the mean values of Q_E during March (Fig. 14c). Notably, an oscillatory pattern in Q_E was observed from 10 to 15 LT during the event, with a minimum at 12 LT (around 154 ± 12 W m^{-2}) and a maximum at 14 LT (close to 212 ± 10 W m^{-2}).

5.6.4. Sensible heat flux (Q_H)

In addition, during intense precipitation events, the maximum peak intensity of Q_H preceded the maximum peak intensity in 10 of 21 events (47.62%). In contrast, for 4 events (19.05%), the maximum peak intensity coincided with the maximum observed in the dry-period, while in 7 events (33.33%) it occurred after the dry-period maximum peak intensity of Q_E. Furthermore, it was also observed that the maximum peak intensity of Q_H surpassed that of the 15 previous days without precipitation as seen in the Figs. 15d and 16d.

The comparison mentioned above of the Q_H for the convective rainfall event ETM_1 (winter season) is shown in Fig. 15d. Precipitation onset at 16:34 LT is marked by a dotted vertical line. Mean Q_H values for the 15 days preceding the event peaked at 14 LT, (approximately 290 ± 21 W m^{-2}). This value is higher than the mean Q_H values at this time in August (Fig. 14d). During the event, Q_H begins to increase significantly from 10 LT reaching its maximum value close to 300 ± 8 at 13 LT. Conversely, for the convective rainfall event ERM_7 (autumn season), shown in Fig. 16d, the maximum Q_H for the 15 preceding days of this event reached maximum values close to 138 ± 10 W m^{-2} at 11 LT similar to the mean values of Q_H during March (Fig. 14d). On the contrary, an oscillatory pattern in Q_H was observed from 10 to 15 LT during the event, with a maximum at 10 LT, close to 130 ± 7 W m^{-2} and minimum at 15 LT, around 23 ± 26 W m^{-2}.

5.6.5. Momentum flux (τ)

In addition, during intense precipitation events, the maximum peak intensity of τ preceded the maximum peak intensity in 09 of 21 events (42.86%). In contrast, for 2 events (9.52%), the maximum peak intensity coincided with the maximum observed in the dry-period, while in 10 events (27.62%) it occurred after the dry-period maximum peak intensity of τ. Furthermore, it was also observed that the maximum τ intensity surpassed that of the 15 previous days without precipitation as seen in the Figs. 15e and 16e.

The comparison mentioned above of τ for the convective rainfall event ETM_1 (winter season) is shown in Fig. 15e. Precipitation onset at 16:34 LT is marked by a dotted vertical line. Mean τ values for the 15 days preceding the event peaked at 16 LT, (approximately 0.20 ± 0.02 m^2 s^{-2}). This value is similar to the mean τ values at this time in August (Fig. 14e). During the event, τ begins to increase significantly from 14 LT reaching its maximum value close to 0.64 ± 0.1 at 16 LT. Conversely, for the convective rainfall event ERM_7 (autumn season), shown in Fig. 16e, the maximum τ for the 15 preceding days of this event reached maximums close to 0.12 ± 0.02 m^2 s^{-2} at 14 LT similar to the mean values of τ during March (Fig. 14e). On the contrary, during the event τ begins to increase significantly from 14 LT reaching its maximum value close to 0.20 ± 0.02 m^2 s^{-2} at 16 LT.

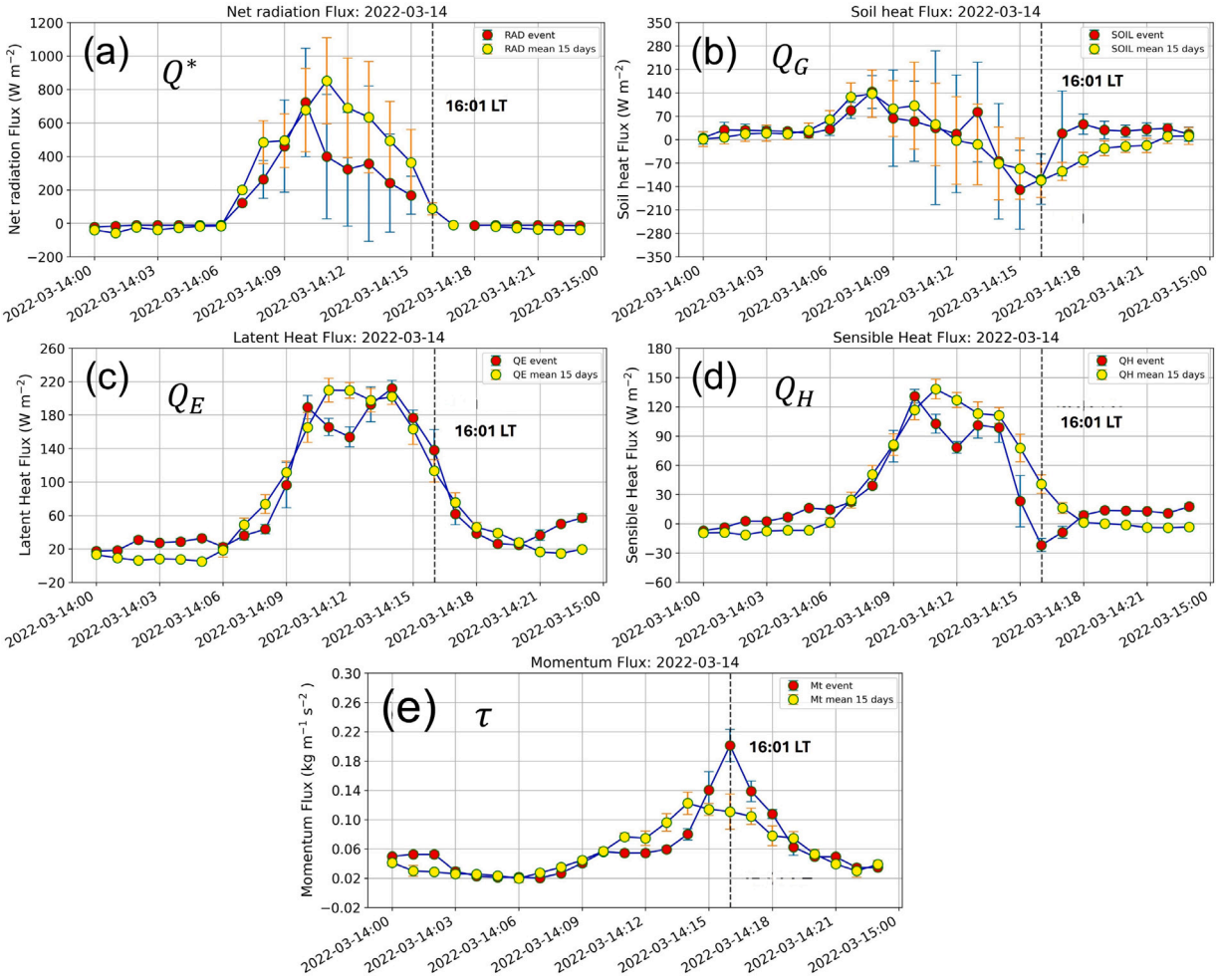

Fig. 16. Daily variation of the SEB components during the intense rainfall event at 14 March, 2022 (ERM_7) and for the previous 15 days without any rainfall conditions. (a) Net irradiance (Q^*), (b) Soil heat flux (Q_G), (c) Latent heat flux (Q_E), (d) Sensible heat flux (Q_H) and (e) Momentum flux (τ). All components are measures in W m^{-2} except for τ which is m^2 s^{-2}. The initial time of the intense rainfall event at 16:01 LT is denoted by the dotted vertical lines.

5.6.6. *SEB components for intense rainfall events*

In this Section we analyzed the behavior of the SEB components during intense rainfall and non-intense rainfall conditions. The first one occurred during transition months (ETM_1) and the other occurred during rainy months (ERM_7). The variation of the SEB components during both conditions can be used as precursor signal for the occurrence of thunderstorm activity.

To demonstrate how the surface energy balance (SEB) affects the physical processes behind intense convective rainfall events at the HYGO, Fig. 17a shows the daily patterns of SEB components during the rainfall event on August 1, 2018 (ETM_1) in the spring season. Beside, Fig. 17b shows the SEB component conditions during the 15 days prior to event ETM_1 without precipitation. A comparison between the two conditions reveals that during the convective event, there are oscillations of Q^*, Q_H and Q_G in the hours before the event due to increased cloud cover. In contrast, the behavior of Q^*, Q_H and Q_G during conditions without precipitation shows a more uniform pattern without oscillations. Besides, both Q^* and Q_H reach their maximum values several hours before the onset of convective precipitation event ETM_1, while Q_G reaches its minimum value a few hours before the event. During the convective event ETM_1, Q_H exhibited higher values, sometimes even approaching the intensity of Q^*. In contrast, latent heat flux (Q_E) showed lower values, but a significant increase in Q_E was observed a few hours before the onset of event ETM_1.

Similarly, Fig. 17c displays the daily variations of surface energy balance (SEB) components during the rainfall event on March 14, 2022 (ERM_7) in the summer season. Fig. 17d shows the SEB component conditions during the 15 days prior to event ERM_7 without precipitation. The behavior is similar to the previous case with oscillations of Q^*, Q_H, Q_G and Q_E in the hours before the event due to increased cloud cover. In contrast, the behavior of Q^*, Q_H and Q_G during conditions without precipitation shows a more uniform pattern without oscillations. However, the convective precipitation event ERM_7 occurred during the summer season, leading to higher maximum intensity of Q^* compared to the previous event ETM_1 occurred in spring. Additionally, the intensity of Q_E surpasses that of Q_H due to the increased evapotranspiration on the HYGO during the summer.

5.7. *Monthly and daily variations of AVG at HYGO*

In this section we presented a detailed description of monthly and daily variations of the mean values of some atmospheric vertical gradients (AVG) at the HYGO between May 2018 and December 2022.

The mean monthly and daily variations for the potential temperature vertical gradient (PTVG) are shown in Fig. 18a. In the austral summer (December-February), the PTVG displays pronounced negative peaks, ranging between −0.32 and −0.40 °C m^{-1} from 11:00 to 13:00 LT, while it nears zero during night hours with slight positive values in the early morning. During the autumn months (March-May), the negative peaks of the PTVG decrease to −0.18 °C m^{-1} in daytime and increase to +0.24 °C m^{-1} at night. This behavior amplifies in winter (June-August), with negative peaks of the PTVG reducing to −0.08 °C

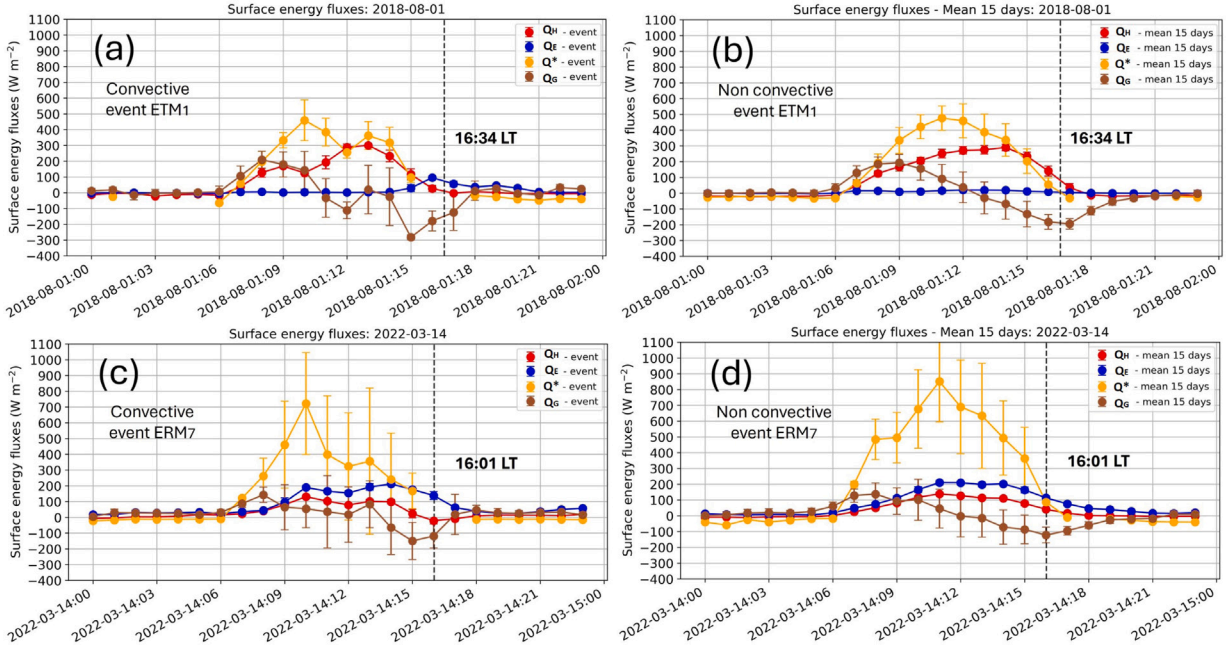

Fig. 17. Daily variation of the SEB components: Net irradiance (Q^*) Soil heat flux (Q_G), Latent heat flux (Q_E) and Sensible heat flux (Q_H) for the (a) convective rainfall event on 01 August, 2018 (ETM_1), (b) during non convective conditions before 15 days of ETM_1, (c) convective rainfall event on 14 March, 2022 (ERM_7) and (d) during non convective conditions before 15 days of ERM_7. The initial times for the intense rainfall events ETM_1 and ERM_7 were 16:34 LT and 16:01 LT, respectively and are indicated by dotted vertical lines.

m^{-1} around noon and positive peaks reaching +0.40 °C m^{-1} in early morning hours. The pattern reverses in spring (September-November), with negative peaks of the PTVG close to −0.24 °C m^{-1} during the day and positive values of around +0.24 °C m^{-1} at night.

Furthermore, the Richardson number (RIN) displays distinct mean monthly and daily variations, as illustrated in Fig. 18b. Across the annual cycle, the RIN predominantly exhibits positive values during nocturnal hours and negative values during diurnal hours. Notably, the highest negative RIN values emerge during winter and spring months, peaking at around −1.6 between 08:00 and 12:00 LT. In contrast, summer and autumn months register comparatively lower negative values, with peaks of up to −1.4 occurring between 08:00 and 12:00 LT. Night hours in autumn, winter, and spring reveal positive RIN values spanning from 0 to 0.2, observed from 19:00 to 06:00 LT. Nevertheless, the summer months present an anomaly, with RIN values ranging from −0.2 to 0 between 00:00 and 05:00 LT.

Moreover, the mean monthly and daily variations for the water mixing vertical gradient (WMVG) are shown in Fig. 18c. The WMVG exhibits marked negative values between January and March, with peaks approximating −0.08 g kg^{-1} m^{-1} observed between 11:00 and 14:00 LT. During night hours, these values moderate, aligning within a range of −0.02 to −0.04 g kg^{-1} m^{-1}. Throughout the autumn months, the negative WMVG peaks subside, eventually transitioning to near-positive values of approximately −0.01 g kg^{-1} m^{-1} during both diurnal and nocturnal periods. This pattern persists into winter, with the WMVG reaching maximum values near +0.03 g kg^{-1} m^{-1} in July around 15:00 LT, while maintaining elevated positive values even during the night. In contrast, the spring months witness a decrease in the WMVG, with it converging toward negative values close to −0.01 g kg^{-1} m^{-1}.

Finally, the horizontal wind vertical gradient (HWVG) exhibits a distinctive pattern across mean monthly and daily variations, as illustrated in Fig. 18d. During the summer months, the HWVG assumes lower values during diurnal hours and higher values throughout the night. Notably, the nocturnal phase registers the most pronounced values, ranging from 0.18 to 0.22 m s^{-1} m^{-1} between 00:00 and 06:00 LT, predominantly during winter. Conversely, the diurnal period in the spring and early summer months sees its highest HWVG values ranging from 0.20 to 0.24 m s^{-1} m^{-1}, particularly between 14:00 and 20:00 LT, with a peak typically observed around 17:00 LT.

5.8. Daily variation of AVG during intense rainfall events at HYGO

The daily variation of atmospheric vertical gradients (PTVG, RIN, WMVG and HWVG) was examined in relation to convective rainfall events at the HYGO location. A comparative analysis was conducted between the AVG variables before, during and after the occurrence of convective rainfall events and the average AVG observed for 15 preceding days devoid of any rainfall conditions. This analysis was performed for the total 21 identified intense rainfall events at HYGO which are shown in Table 7 for PTVG and RIN and in Table 8 for WMVG and HWVG.

5.8.1. Potential temperature vertical gradient (PTVG) and richardson number (RIN)

In the case of the most intense precipitation events, it was observed that both the minimum PTVG intensity (Fig. 19a) and the minimum RIN intensity (Fig. 19b) during these events exceeded that of the respective 15 previous days with no precipitation. This phenomenon is also illustrated for a different time period in Fig. 20a for PTVG and in Fig. 20b for RIN.

Figs. 19a and 20a offer a comparative analysis of PTVG during two separate convective rainfall events: one on August 1, 2018 (ETM_1) in the winter season and another on March 14, 2022 (ERM_7) in the autumn season. In both cases, PTVG exhibited a similar pattern, with its minimum value occurring during the respective rainfall events. During the event ETM_1, PTVG dipped to −0.19 ± 0.05 around 13 LT, while the 15-day period preceding the event showed a mean PTVG of −0.18 ± 0.05 at 11 LT. These values exceeded the baseline PTVG intensity for August, which averages around −0.16, as illustrated in Fig. 18a. Similarly, during the event ERM_7, PTVG reached its minimum value of −0.37 ± 0.12 around 14 LT, with the 15-day period leading up to the event demonstrating a minimum mean PTVG of −0.36 ± 0.09 at 11 LT. Once again, both of these values surpassed the baseline PTVG intensity for March, which is approximately −0.32, as shown in Fig. 18a. These distinct behaviors highlight the impact of convective rainfall events on PTVG intensity.

Additionally, Figs. 19b and 20b present a comparative analysis of RIN during the same two convective rainfall events. In both instances,

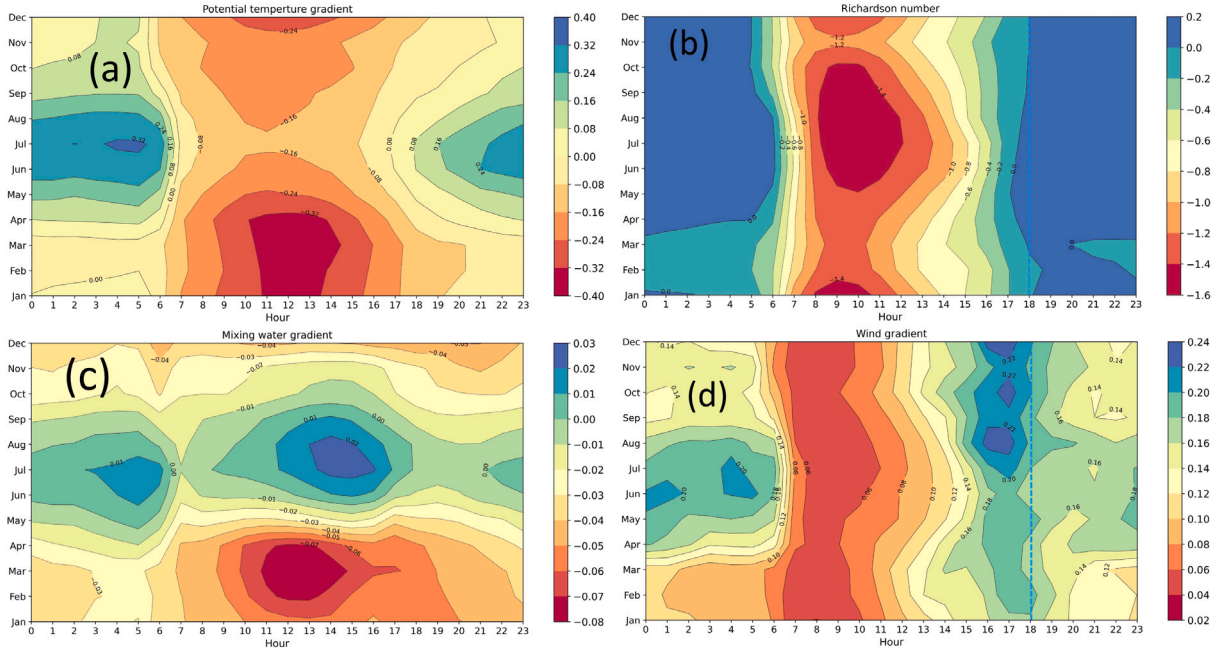

Fig. 18. Monthly and daily variations of mean AVG between May 2018 and December 2022. The variables shown are: (a) PTVG (°C m^{-1}), (b) RIN, (c) WMVG (g kg^{-1} m^{-1}) and (d) HWVG (m s^{-1} m^{-1}). The behavior of theses variables during the maximum hourly mean precipitation at the HYGO at 18 LT, is illustrated by the vertical dotted lines.

Table 7
Potential temperature gradient (PTVG) and Richardson number (RIN) during the intense rainfall events identified at the HYGO and for 15 preceding days devoid of any rainfall conditions. The analysis focused on two groups: the first comprised 14 events during transition months (ETM) (spring and autumn), while the second consisted of 7 events during rainy months (ERM) (summer). In total, 21 convective activity-associated rainfall events were identified.

Event	Onset rainfall (LT)	PTG (K m^{-1})				RiN			
		Day event		15 days before		Day event		15 days before	
		Hour Max	Value Max	Hour Max	Value Max	Hour Min	Value Min	Hour Min	Value Min
Events in transition months (ETM)									
ETM_1	16:34 LT	13 LT	−0.19 ± 0.05	14 LT	−0.18 ± 0.05	10 LT	−1.73 ± 0.03	10 LT	−1.65 ± 0.05
ETM_2	17:06 LT	11 LT	−0.24 ± 0.05	11 LT	−0.19 ± 0.05	09 LT	−1.77 ± 0.10	10 LT	−1.67 ± 0.05
ETM_3	16:13 LT	10 LT	−0.29 ± 0.05	10 LT	−0.17 ± 0.04	09 LT	−1.72 ± 0.07	09 LT	−1.74 ± 0.03
ETM_4	16:59 LT	13 LT	−0.37 ± 0.09	12 LT	−0.21 ± 0.05	09 LT	−2.0 ± 0.05	09 LT	−1.77 ± 0.04
ETM_5	18:05 LT	13 LT	−0.49 ± 0.13	12 LT	−0.36 ± 0.10	08 LT	−1.69 ± 0.03	08 LT	−1.59 ± 0.05
ETM_6	18:18 LT	11 LT	−0.40 ± 0.10	12 LT	−0.34 ± 0.10	08 LT	−1.72 ± 0.03	08 LT	−1.64 ± 0.05
ETM_7	14:36 LT	16 LT	−0.66 ± 0.29	13 LT	−0.43 ± 0.13	08 LT	−1.73 ± 0.02	10 LT	−1.55 ± 0.05
ETM_8	17:06 LT	12 LT	−0.56 ± 0.14	12 LT	−0.42 ± 0.12	07 LT	−1.62 ± 0.10	10 LT	−1.61 ± 0.05
ETM_9	15:21 LT	13 LT	−0.22 ± 0.05	11 LT	−0.17 ± 0.05	09 LT	−1.78 ± 0.01	09 LT	−1.55 ± 0.06
ETM_{10}	17:00 LT	11 LT	−0.14 ± 0.10	11 LT	−0.12 ± 0.05	11 LT	−1.58 ± 0.03	10 LT	−1.55 ± 0.04
ETM_{11}	16:28 LT	15 LT	−0.16 ± 0.08	11 LT	−0.13 ± 0.05	11 LT	−1.66 ± 0.04	10 LT	−1.52 ± 0.04
ETM_{12}	16:50 LT	11 LT	−0.20 ± 0.10	10 LT	−0.16 ± 0.04	12 LT	−1.50 ± 0.01	10 LT	−1.58 ± 0.06
ETM_{13}	17:49 LT	12 LT	−0.23 ± 0.07	12 LT	−0.26 ± 0.06	13 LT	−1.61 ± 0.07	10 LT	−1.47 ± 0.06
ETM_{14}	18:09 LT	13 LT	−0.58 ± 0.14	13 LT	−0.38 ± 0.09	11 LT	−1.44 ± 0.06	09 LT	−1.08 ± 0.04
Events in rainy months (ERM)									
ERM_7	17:40 LT	13 LT	−0.48 ± 0.12	10 LT	−0.32 ± 0.10	09 LT	−1.86 ± 0.02	10 LT	−1.73 ± 0.09
ERM_2	16:32 LT	13 LT	−0.57 ± 0.16	12 LT	−0.51 ± 0.13	10 LT	−1.81 ± 0.10	09 LT	−1.38 ± 0.08
ERM_3	14.26 LT	12 LT	−0.53 ± 0.14	12 LT	−0.48 ± 0.13	07 LT	−1.78 ± 0.12	09 LT	−1.46 ± 0.07
ERM_4	18:17 LT	13 LT	−0.63 ± 0.15	12 LT	−0.47 ± 0.13	05 LT	−1.40 ± 0.15	09 LT	−1.46 ± 0.08
ERM_5	16:54 LT	15 LT	−0.38 ± 0.08	13 LT	−0.30 ± 0.07	10 LT	−1.38 ± 0.02	10 LT	−1.20 ± 0.05
ERM_6	18:13 LT	12 LT	−0.42 ± 0.12	13 LT	−0.30 ± 0.09	10 LT	−1.86 ± 0.04	09 LT	−1.66 ± 0.06
ERM_7	16:01 LT	14 LT	−0.37 ± 0.12	11 LT	−0.36 ± 0.09	05 LT	−1.40 ± 0.09	09 LT	−1.16 ± 0.05

RIN exhibited a similar trend, reaching its minimum value during the respective rainfall events. Specifically, during the event ETM_1, RIN dipped to −1.73 ± 0.03 around 10 LT, while the 15 days leading up to the event showed a mean RIN of −1.65 ± 0.05 at 10 LT, surpassing the baseline RIN intensity for August, which averages around −1.4, as depicted in Fig. 18b. Likewise, during the event ERM_7, RIN reached its minimum value of −1.30 ± 0.09 around 11 LT, with the 15-day period prior to the event demonstrating a minimum mean RIN of −1.16 ± 0.05 at 11 LT, exceeding the baseline RIN intensity for March, which is approximately −1.2, as illustrated in Fig. 18b. This consistent behavior underscores the influence of convective rainfall events on RIN intensity.

5.8.2. Water vapor vertical gradient (WMVG) and horizontal wind vertical gradient (HWVG)

During the most intense precipitation events, both the minimum WMVG intensities and the maximum HWVG intensities, exceeded the values observed during the preceding 15-day period without precipitation. For instance, Figs. 19c and 20c provide a comparative analysis of

Table 8
Water vapor mixing ratio gradient (WMVG) and wind velocity gradient (HWVG) during the intense rainfall events identified at the HYGO and for 15 preceding days devoid of any rainfall conditions. The analysis focused on two groups: the first comprised 14 events during transition months (ETM) (spring and autumn), while the second consisted of 7 events during rainy months (ERM) (summer). In total, 21 convective activity-associated rainfall events were identified.

Event	Onset	WMVG (g kg^{-1}/m)				HWVG (m s^{-1}/m)			
	rainfall (LT)	Day event		15 days before		Day event		15 days before	
		Hour Max	Value Max	Hour Max	Value Max	Hour Min	Value Min	Hour Min	Value Min
Events in transition months (ETM)									
ETM_1	16:34 LT	16 LT	−0.041 ± 0.013	07 LT	−0.006 ± 0.05	16 LT	0.62 ± 0.18	17 LT	0.27 ± 0.08
ETM_2	17:06 LT	17 LT	−0.043 ± 0.021	07 LT	−0.007 ± 0.05	17 LT	0.31 ± 0.24	17 LT	0.26 ± 0.08
ETM_3	16:13 LT	16 LT	−0.030 ± 0.042	07 LT	+0.003 ± 0.007	16 LT	0.46 ± 0.10	17 LT	0.25 ± 0.08
ETM_4	16:59 LT	17 LT	−0.038 ± 0.028	19 LT	−0.011 ± 0.015	16 LT	0.28 ± 0.14	17 LT	0.23 ± 0.08
ETM_5	18:05 LT	16 LT	−0.079 ± 0.044	12 LT	−0.054 ± 0.030	13 LT	0.34 ± 0.14	18 LT	0.21 ± 0.10
ETM_6	18:18 LT	16 LT	−0.097 ± 0.024	20 LT	−0.055 ± 0.027	15 LT	0.23 ± 0.07	18 LT	0.24 ± 0.11
ETM_7	14:36 LT	13 LT	−0.10 ± 0.041	13 LT	−0.084 ± 0.041	14 LT	0.28 ± 0.12	18 LT	0.20 ± 0.10
ETM_8	17:06 LT	12 LT	−0.103 ± 0.036	12 LT	−0.082 ± 0.038	17 LT	0.31 ± 0.12	18 LT	0.22 ± 0.09
ETM_9	15:21 LT	15 LT	−0.002 ± 0.030	06 LT	−0.008 ± 0.010	15 LT	0.30 ± 0.27	17 LT	0.25 ± 0.08
ETM_{10}	17:00 LT	17 LT	−0.050 ± 0.030	06 LT	−0.013 ± 0.018	17 LT	0.29 ± 0.19	16 LT	0.21 ± 0.08
ETM_{11}	16:28 LT	16 LT	−0.041 ± 0.040	06 LT	−0.017 ± 0.019	15 LT	0.29 ± 0.10	23 LT	0.20 ± 0.08
ETM_{12}	16:50 LT	09 LT	−0.022 ± 0.019	07 LT	−0.022 ± 0.012	16 LT	0.23 ± 0.08	17 LT	0.22 ± 0.08
ETM_{13}	17:49 LT	17 LT	−0.019 ± 0.042	21 LT	−0.056 ± 0.028	17 LT	0.23 ± 0.10	16 LT	0.22 ± 0.08
ETM_{14}	18:09 LT	13 LT	−0.141 ± 0.047	13 LT	−0.093 ± 0.029	18 LT	0.26 ± 0.12	13 LT	0.18 ± 0.10
Events in rainy months (ERM)									
ERM_1	17:40 LT	13 LT	−0.113 ± 0.038	01 LT	−0.121 ± 0.045	17 LT	0.38 ± 0.18	12 LT	0.10 ± 0.06
ERM_2	16:32 LT	13 LT	−0.116 ± 0.052	12 LT	−0.110 ± 0.041	15 LT	0.38 ± 0.10	16 LT	0.26 ± 0.10
ERM_3	14.26 LT	12 LT	−0.112 ± 0.041	12 LT	−0.102 ± 0.039	14 LT	0.42 ± 0.18	17 LT	0.25 ± 0.08
ERM_4	18:17 LT	13 LT	−0.134 ± 0.043	12 LT	−0.100 ± 0.038	18 LT	0.20 ± 0.13	16 LT	0.25 ± 0.09
ERM_5	16:54 LT	17 LT	−0.075 ± 0.026	13 LT	−0.041 ± 0.018	17 LT	0.35 ± 0.17	17 LT	0.18 ± 0.08
ERM_6	18:13 LT	12 LT	−0.092 ± 0.040	18 LT	−0.053 ± 0.023	18 LT	0.21 ± 0.10	17 LT	0.15 ± 0.05
ERM_7	16:01 LT	16 LT	−0.113 ± 0.028	11 LT	−0.083 ± 0.031	16 LT	0.35 ± 0.15	16 LT	0.18 ± 0.08

WMVG during two convective rainfall events: one on August 1, 2018 (ETM_1) in the winter season and another on March 14, 2022 (ERM_7) in the autumn season. In both cases, WMVG exhibited a similar pattern, with its minimum value occurring during the respective rainfall events. During the event ETM_1, WMVG dipped to −0.041 ± 0.013 around 16 LT, while the 15-day period preceding the event showed a mean WMVG of −0.006 ± 0.05 at 07 LT. These values exceeded the baseline WMVG intensity for August, which averages around +0.01, as depicted in Fig. 18c. Similarly, during the event ERM_7, WMVG reached its minimum value of −0.113 ± 0.028 around 13 LT, with the 15-day period leading up to the event demonstrating a minimum mean WMVG of −0.083 ± 0.031 at 11 LT, surpassing the baseline WMVG intensity for March, which is approximately −0.07, as shown in Fig. 18c. This consistent behavior highlights the impact of convective rainfall events on WMVG intensity.

Additionally, Figs. 19d and 20d present a comparative analysis of HWVG during the same two convective rainfall events. In both instances, HWVG exhibited a similar trend, with its maximum value occurring during the respective rainfall events. Specifically, during the event ETM_1, HWVG reached its maximum value of 0.62 ± 0.18 around 16 LT, while the 15 days leading up to the event showed a mean HWVG of 0.27 ± 0.08 at 17 LT. Both of these values exceeded the baseline HWVG intensity for August, which averages around +0.01, as illustrated in Fig. 18d. Likewise, during the event ERM_7, HWVG reached its minimum value of 0.35 ± 0.15 around 16 LT, with the 15-day period prior to the event demonstrating a minimum mean HWVG of 0.18 ± 0.08 at 16 LT. The former value surpassed the baseline HWVG intensity for March, which is approximately 0.22, as illustrated in Fig. 18d. This consistent behavior underscores the influence of convective rainfall events on HWVG intensity.

To demonstrate how the atmospheric vertical gradients (AVG) affects the physical processes behind intense convective rainfall events at the HYGO, Fig. 21a shows the daily patterns of AVG components during the rainfall event on August 1, 2018 (ETM_1) in the spring season. Besides, Fig. 21b shows the AVG component conditions during the 15 days prior to event ETM_1 without precipitation. A comparison between the two conditions shows a significant increase in HWVG and a notable decrease in WMVG several minutes just before the onset of convective event ETM_1. In contrast, these variables showed a smoother variation during non-convective conditions throughout the daily variations. Besides, was observed a notable increase of the PTVG several hours to the onset of the precipitation event ETM_1; meanwhile presented a more smoothed variation during non convective conditions.

Similarly, Fig. 21c displays the daily variations of atmospheric vertical gradients (AVG) during the rainfall event on March 14, 2022 (ERM_7) in the summer season. Fig. 21d shows the AVG conditions during the 15 days prior to event ERM_7 without precipitation. The behavior is similar to the previous case, but with lower values for maximum peaks of HWVG and minimum peaks of WMVG. Besides, the PTVG presents lower minimum peaks compared with the previous event, indicating more unstable conditions during the summer.

6. Discussions

This study aimed to deepen our understanding of precipitation dynamics, surface energy exchanges, and atmospheric stability conditions driving intense convective rainfall in the Central Andes. To achieve this, we analyzed long-term climate data (1965–2018) alongside high-resolution, event-specific data (2018–2022) and evaluated the performance of the Advanced Regional Prediction System (ARPS) model. In the sections that follow, we discuss our findings in direct relation to the study's objectives.

6.1. Rainfall characteristics

Our analysis of one-minute rainfall data (2018–2022) reveals distinct daily and seasonal precipitation patterns. Daily rainfall peaks were typically observed around 1800 local time, with significant events clustering between 14:00 and 22:00 LT. Seasonally, the data show dry intervals from April to August and rainy seasons from September to March. These patterns align well with the long-term (1965–2018) climate-scale observations, which also indicate elevated precipitation from January to March and reduced rainfall from May to July. Furthermore, the identification of 21 intense rainfall events linked to

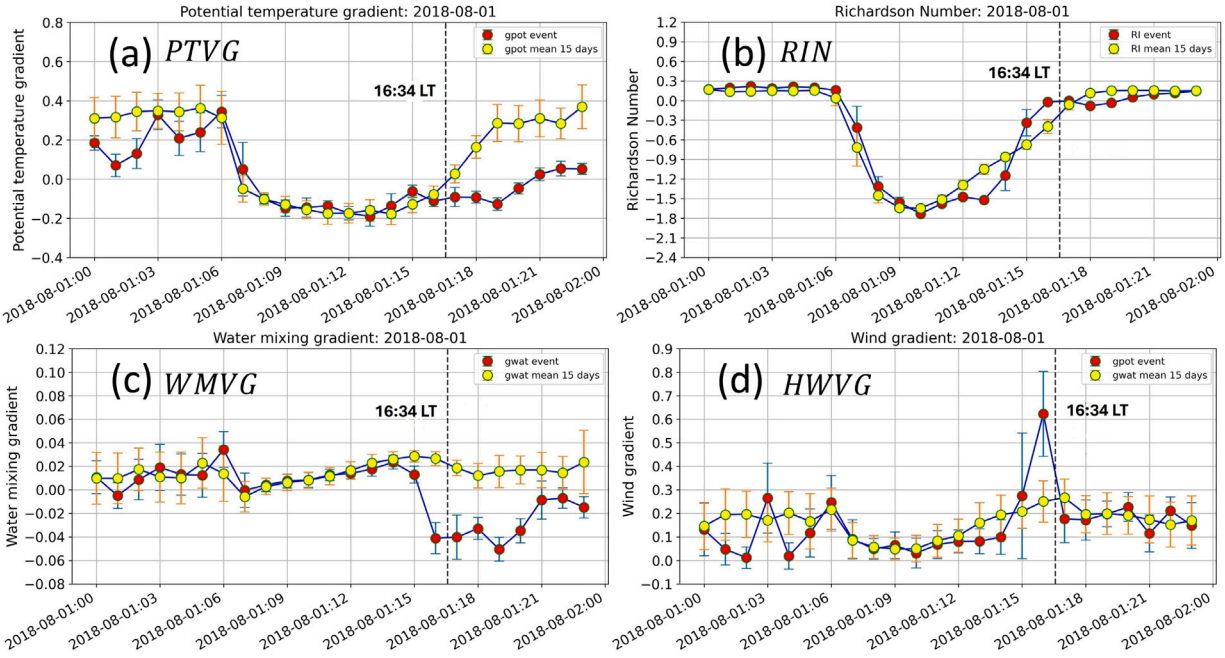

Fig. 19. Daily variations of the AVG components during the intense rainfall event at 01 August, 2018 (ETM_1) and for the previous 15 days without any rainfall conditions. (a) PTVG (°C m^{-1}), (b) RIN, (c) WMVG (g kg^{-1} m^{-1}), and (d) HWVG (m s^{-1} m^{-1}). The initial time of the intense rainfall event at 16:34 LT is denoted by the dotted vertical lines.

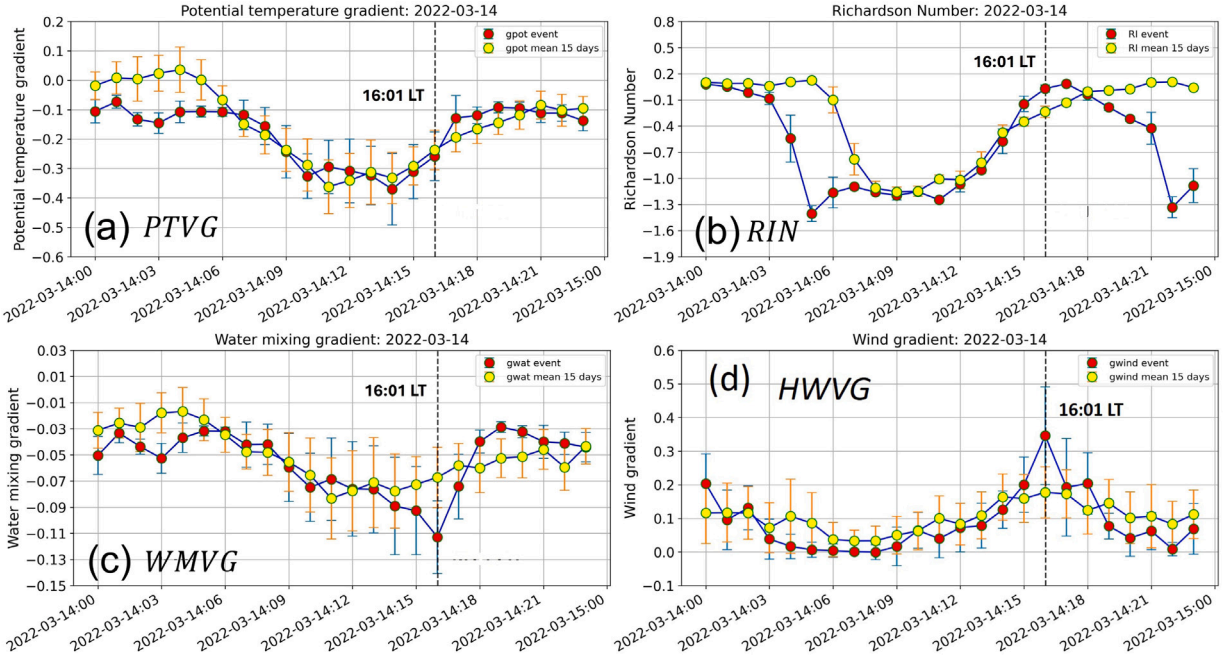

Fig. 20. Daily variation of the AVG components during the intense rainfall event at 14 March, 2022 (ERM_7) and for the previous 15 days without any rainfall conditions. PTVG (°C m^{-1}), (b) RIN, (c) WMVG (g kg^{-1} m^{-1}), and (d) HWVG (m s^{-1} m^{-1}). The initial time of the intense rainfall event at 16:01 LT is denoted by the dotted vertical lines.

convective activity provides valuable insights into the synoptic and mesoscale drivers influencing these episodes. This dual approach — comparing long-term trends with high-resolution event-specific observations — strengthens our understanding of both the background climatology and the mechanisms triggering extreme events. It is important to highlight that most of the intense precipitation events were recorded during the transition months between dry and rainy periods, that is, during the late winter and early spring, and in the late summer and early autumn.

To identify extreme precipitation events linked to convective activity, we conducted an extensive boxplot analysis of hourly precipitation data at HYGO from 2018 to April 2022. Outliers, indicating significant deviations from typical precipitation, served as indicators of severe weather conditions. The period from 2019 to 2020 saw a marked decrease in both the frequency and intensity of precipitation events, possibly influenced by the La Niña event, as indicated by the Oceanic Niño Index (ONI), suggesting its role in the observed reduction in intense precipitation events. In addition, we used key precipitation variables as reflectivity and vertical velocity, obtained from the MIRA-35c vertical profiler radar and GPM-IMERG rainfall estimation products. These variables are crucial for detecting extreme precipitation events associated with convective activity. Based on specific criteria

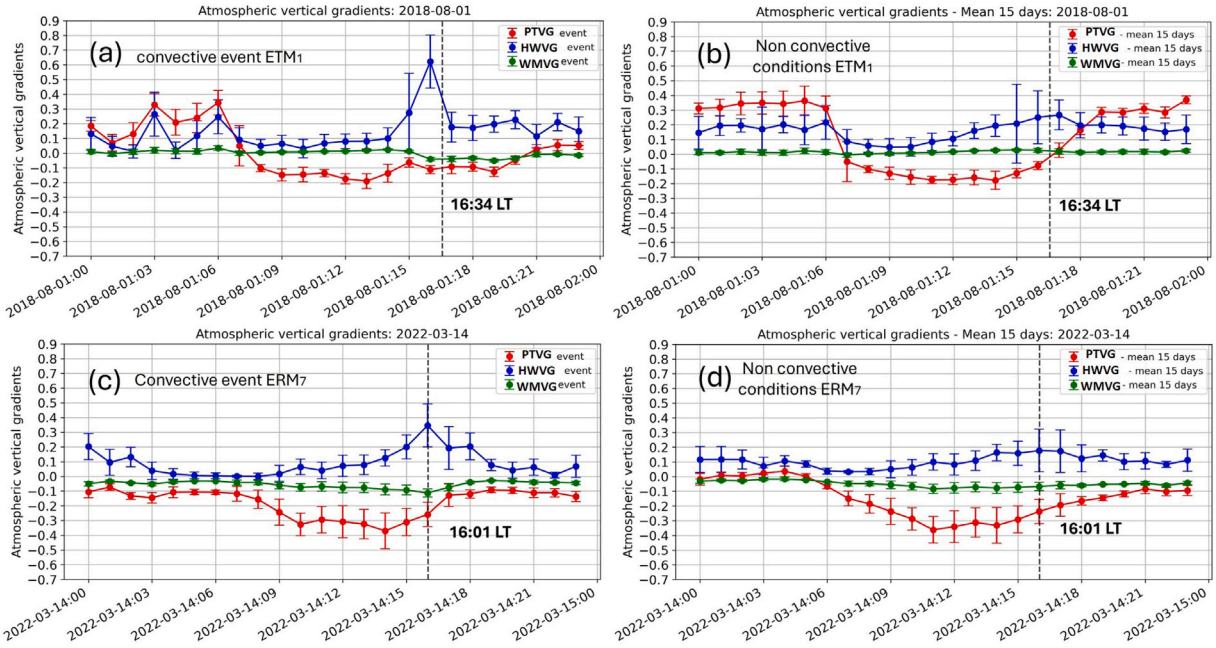

Fig. 21. Daily variation of the AVG components: PTVG, WMVG and HWVG for the (a) convective rainfall event on 01 August, 2018 (ETM_1), (b) during non convective conditions before 15 days of ETM_1, (c) convective rainfall event on 14 March, 2022 (ERM_7) and (d) during non convective conditions before 15 days of ERM_7. The initial times for the intense rainfall events ETM_1 and ERM_7 were 16:34 LT and 16:01 LT, respectively and are indicated by dotted vertical lines.

and data collected from pluviometer, MIRA-35c radar, and GPM-IMERG products, a comprehensive analysis identified 21 intense precipitation events linked to convective activity spanning from 2018 to 2022.

6.2. Simulation of turbulent energy fluxes

We conducted numerical simulations using the ARPS model at a 0.5-km resolution to analyze turbulent energy fluxes (Q_H and Q_E) during 21 extreme rainfall events at HYGO. Comparisons between the ARPS outputs and estimates from the bulk aerodynamic method (at a 1 min resolution) reveal that the ARPS model generally underestimates Q_H for fluxes up to 450 W m^{-2} (R^{-2} = 0.56). In contrast, for Q_E the model tends to overestimate low values but converges toward Q_H-like behavior at higher fluxes (R^{-2} = 0.24).

For most events, simulated Q_H values fall short of the aerodynamic estimates, though two exceptional cases during late summer and early autumn showed higher ARPS values. Similarly, while ARPS QQ_E values were typically lower than the aerodynamic method's estimates, eight instances during late winter and early spring exhibited higher values. These findings highlight the need for further calibration of the ARPS model, particularly its drag and exchange coefficients, and for updating satellite-derived soil and surface cover data. Such improvements are essential to enhance the model's predictive accuracy for convective precipitation in the Central Andes.

These results underscore the necessity of conducting a study to calibrate both the models and the drag and exchange coefficients of the surface employed by the ARPS model for estimating surface energy fluxes in the Central Andes region of Peru. Furthermore, there is a need for updating the data regarding soil types and surface cover types obtained through satellite information. This calibration and data update study is crucial for enhancing the predictive capacity of convective precipitation forecasts by the ARPS model.

6.3. Daily variation of SEB components during intense rainfall events at HYGO

During convective rainfall events at HYGO, distinct patterns emerge in the daily evolution of energy flux components, offering valuable insights into the processes that precede intense rainfall. In the transition from the dry season (winter) to the rainy season (spring), the atmospheric conditions are initially characterized by low average latent heat flux (Q_E) values. However, in the hours leading up to convective precipitation, a marked surge in Q_E is observed. This abrupt increase contrasts sharply with the preceding 15-day period, during which Q_E remains relatively low. As Q_E intensifies, the net available energy (Q^*) becomes partitioned in a nearly equal manner among Q_E, sensible heat flux (Q_H), and ground heat flux (Q_G). In non-event periods, Q^* is primarily allocated to Q_H, followed by Q_G and then Q_E, indicating a more stable energy balance when convective triggers are absent.

The rapid enhancement of Q_E not only signals the mobilization of latent energy but also aligns with a significant increase in horizontal momentum flux (τ). The rise in τ suggests enhanced wind shear and dynamic forcing, both of which contribute to boundary layer destabilization. Together, these changes in Q_E and τ serve as early-warning indicators — precursor variables — that flag the imminent onset of convective rainfall during the winter–spring transition. A contrasting behavior is evident during the transition from the rainy season (summer) to the dry season (autumn). In this period, the baseline Q_E is moderately high, yet the pre-event signature differs. Here, the hours preceding a convective event show only a modest increase in Q_E. Instead, a notable decline in Q_H is observed, likely influenced by an increased cloud cover that reduces Q^*. In this scenario, Q^* continues to be partitioned relatively evenly among Q_E, Q_H, and Q_G; however, the overall decrease in Q^* and the accompanying drop in Q_H intensity indicate a different modulation of surface energy exchanges compared to the winter–spring period. Despite these variations, horizontal momentum flux (τ) consistently exhibits a pronounced increase prior to convective events during the summer–autumn transition, reinforcing its role as a robust precursor signal.

Furthermore, the behavior of Q_H and Q_G during both transitions reinforces their importance in pre-convective dynamics. In the hours before rainfall, Q_H and Q_G display more pronounced peaks — Q_H trending positively and Q_G negatively — when compared to their 15-day averages during non-event conditions. This enhanced variability underscores the sensitivity of these fluxes to subtle changes in surface

heating and cooling processes that are critical for triggering convective instability.

Overall, the contrasting patterns in the evolution of Q^*, Q_E, Q_H, Q_G, and τ across the two seasonal transitions provide a comprehensive picture of the complex interplay between surface energy fluxes and atmospheric dynamics. During the winter–spring transition, the sharp rise in Q_E and τ clearly marks the approach of convective activity, while in the summer–autumn transition, the combined effect of diminished Q^* and Q_H — coupled with an increase in τ — highlights a different set of thermodynamic adjustments preceding precipitation. These findings not only enhance our understanding of convective processes at HYGO but also offer practical insights for the refinement of predictive models, enabling more accurate anticipation of extreme weather events during critical seasonal shifts.

6.4. Daily variation of AVG during intense rainfall events at HYGO

The vertical gradients of key atmospheric variables — water vapor mixing ratio (WMVG), horizontal wind (HWVG), potential temperature (PTVG), and the Richardson number (RIN) — are analyzed as indicators for the onset of convective precipitation.

During convective events in the winter–spring transition at HYGO, when the average WMVG is positive, a notable decline in WMVG is observed in the hours preceding intense rainfall. This decline shifts WMVG to moderately negative values, contrasting with the stable, positive values seen during the 15 days without significant precipitation. Such a shift indicates a dynamic reorganization of surface moisture fluxes, enhancing atmospheric buoyancy and contributing to the initiation of convection.

A similar pattern is seen in the behavior of RIN. Average RIN values during this period are moderately negative, and a further perceptible decrease occurs just before convective events, again contrasting with the more stable values observed during non-event periods. In contrast, the potential temperature gradient (PTVG) exhibits little variation in the hours before convective onset; however, its consistently negative values underscore the dominant role of sensible heat flux from the surface in generating buoyancy.

In addition, the horizontal wind gradient (HWVG) increases significantly in the hours leading up to convective precipitation, reaching its highest seasonal values compared to other months. This pronounced increase in HWVG, closely associated with the dynamics of horizontal momentum flux (τ), reinforces its value as a robust precursor.

During the summer–autumn transition, while the overall behavior of these vertical gradients is similar, the mean WMVG exhibits a more marked decrease, suggesting an even more substantial transport of surface moisture during these months. Together, these variations in WMVG, RIN, PTVG, and HWVG provide valuable insights into the evolving boundary layer conditions and offer promising signals for forecasting convective precipitation events at HYGO.

6.5. Final considerations

Our findings align with many of the behaviors reported in other regions, yet they also offer unique insights. For instance, like many studies (Raman et al., 1998; Venalainen et al., 1998), we observe that an increase in latent heat Q_E and a shift toward a more balanced energy partitioning serve as precursors to convective precipitation. In our work—building on the framework of Tyagi and Satyanarayana (2015) and Satyanarayana et al. (2014) we found that, during intense convective events, Q_E increases significantly, sometimes even exceeding Q_H, while non-convective periods show a dominance of Q_H. This behavior is consistent with observations elsewhere that highlight the role of moisture availability and boundary layer buoyancy in storm initiation.

However, there are some distinctions in our results that can be attributed to local conditions. For example, the magnitude and timing of the flux shifts (with pronounced changes in the hours preceding convective events) in our HYGO dataset differ from observations in other regions, possibly due to differences in soil moisture, vegetation cover, and the unique diurnal heating patterns of the study area. Furthermore, our integrated analysis — combining high-resolution rainfall data, numerical simulations (using the ARPS model), and detailed vertical gradient measurements — provides a more nuanced picture of the physical mechanisms at play. In particular, the simultaneous increase in horizontal momentum flux (τ) and the observed changes in vertical gradients of WMVG and RIN complement the traditional surface flux perspective, offering additional predictors of convective activity.

In summary, while the physical mechanisms — such as enhanced latent energy availability and boundary layer instability — are common across different regions, our study highlights region-specific features (e.g., the precise timing and magnitude of these changes) that refine our understanding of convective precursors. This detailed, multi-scale approach not only corroborates established observations in the literature but also extends them by emphasizing the interplay between surface energy partitioning and atmospheric dynamics in the HYGO region.

7. Conclusions

This study provides a detailed examination of precipitation dynamics, surface energy exchanges, and atmospheric stability indicators in the HYGO region of the Central Andes, offering significant advancements in our understanding of convective precipitation processes. High-resolution one-minute rainfall data (2018–2022) reveal that peak precipitation typically occurs between 14:00 and 22:00 LT, while seasonal patterns indicate dry intervals from April to August and rainy periods from September to March. The identification of 21 intense convective precipitation events — primarily during the transition months of late winter–early spring and late summer–early autumn — highlights the influence of both synoptic-scale and mesoscale drivers in triggering extreme weather events.

Numerical simulations at a 0.5-km resolution using the ARPS model show that the model generally underestimates sensible heat flux (Q_H) relative to bulk aerodynamic estimates (with an R^2 of 0.56) and exhibits mixed performance for latent heat flux (Q_H), depending on flux magnitude. These discrepancies underscore the need to refine the ARPS model — particularly through the recalibration of drag and exchange coefficients and updating satellite-derived soil and vegetation data — to improve its accuracy in estimating surface energy fluxes under convective conditions.

Analysis of daily variations in surface energy balance reveals that a rapid increase in Q_E and a concurrent rise in horizontal momentum flux (τ) serve as early indicators of impending convective precipitation. This shift in energy partitioning — from a dominant allocation to Q_H during non-event periods to a nearly equal division among Q_E, Q_H, and Q_G prior to events — is particularly pronounced during the winter–spring transition. In parallel, vertical gradients of key atmospheric variables, such as water vapor mixing ratio (WMVG), horizontal wind (HWVG), potential temperature (PTVG), and the Richardson number (RIN), exhibit distinct pre-convective behavior. A decline in WMVG and a more negative RIN, together with pronounced peaks in HWVG, are observed in the hours preceding convective events, providing robust precursor signals critical for forecasting.

The combined insights from these analyses contribute to a more comprehensive understanding of convective processes in the region. By integrating these precursor signals and refining model calibrations, future predictive frameworks can be significantly improved, leading to more accurate early warning systems for convective rainfall events in mountainous regions—a vital step for disaster preparedness in the Central Andes. Overall, this research not only deepens our fundamental understanding of convective precipitation at HYGO but also lays the groundwork for enhanced forecasting capabilities through improved

numerical modeling and the integration of early-warning indicators that can be used in machine learning techniques to forecast intense rainfall convective events.

For instance, Kiranyaz et al. (2021) shows that Convolutional Neural Networks (CNNs) have become the standard for many machine learning tasks, typically involving complex visual data. While 2D CNNs dominate in image analysis, the emergence of simplified 1D CNNs has opened promising avenues for applications involving one-dimensional signals. Due to their compact structure and efficient real-time processing, 1D CNNs can effectively address scenarios where data availability is limited or highly specialized, such as surface energy flux analysis and the forecasting of convective rainfall events. These neural networks demonstrate state-of-the-art performance in anomaly detection and classification tasks, making them particularly suitable for real-time environmental monitoring, meteorological forecasting, and early warning systems.

CRediT authorship contribution statement

José Luis Flores-Rojas: Visualization, Validation, Supervision, Methodology, Investigation, Formal analysis, Data curation, Conceptualization. **David A. Guizado-Vidal:** Investigation, Data curation. **Jairo Valdivia-Prado:** Formal analysis, Data curation. **Yamina Silva:** Resources, Methodology, Funding acquisition. **Elver Villalobos-Puma:** Investigation, Formal analysis, Conceptualization. **Luis Suárez-Salas:** Investigation, Conceptualization. **Zenón Mata-Adauto:** Resources, Funding acquisition. **Hugo Abi Karam:** Methodology, Investigation, Formal analysis, Conceptualization.

Declaration of competing interest

The authors declare no conflict of interest.

Acknowledgments

We gratefully acknowledge the support of the LAMAR project, "Fortalecimiento del Laboratorio de Microfísica Atmosférica *y* Radiación para el estudio de la interacción superficie-atmósfera en una zona agrícola de los Andes Centrales del Perú, en el contexto de cambio climático", CONTRATO N° PE501086050-2023-PROCIENCIA-BM. This initiative, funded by the Programa Nacional de Investigación Científica *y* Estudios Avanzados (PROCIENCIA) and supported by the Instituto Geofísico del Perú, has been instrumental in advancing our research. Also, we wish to thank to the "PROCIENCIA" (N° PE501080424- 2022-PROCIENCIA) for the financial support during the research period, in the context to the project: Biomass Burning and Impacts in the Southern Tropics with financial scheme E070-2022-01. In addition, this work was done using computational resources, HPC-Linux-Cluster, from "Laboratorio de Dinámica de Fluidos Geofísicos Computacionales at Instituto Geofísico del Perú" (grants 101-2014-FONDECYT, SPIRALES2012 IRD-IGP, Manglares IGP-IDRC, PP068 program). Finally, we want to thanks to the AI of ChatGPT which only was used to improve the English style of the manuscript.

Data availability

Data will be made available on request.

References

Arya, S., 1998. Introduction to Micrometeorology, second ed. Academic Press.
Beringer, J., Tapper, N., 2000. The influence of subtropical cold fronts on the surface energy balance of a semi-arid site. J. Arid. Environ. 44, 437–450.
Beringer, J., Tapper, N., 2002. Surface energy exchanges and interactions with thunderstorms during the Maritime Continent Thunderstorm Experiment (MCTEX). J. Geophys. Res.: Atmospheres 107, D21.
Bhat, G., Arunchandra, S., 2008. On the measurement of the surface energy budget over the land surface during the summer monsoon. J. Earth. Syst. Sci. 117 (6), 911–923.
Businger, J., Wyngaard, J., Izumi, Y., Bradley, E., 1971. Flux-profile relationships in the atmospheric surface layer. J. Atmos. Sci. 28, 181–189.
Byun, D., 1990. On the analytical solutions of flux-profile relationships for the atmospheric surface layer. J. Appl. Meteorol. 29, 652–657.
Callanaupa, S., Segura, C., Saavedra, H., Flores-Rojas, J., Silva, Y., Cuxart, J., 2021. Seasonal variability of daily evapotranspiration and energy fluxes in the Central Andes of Peru using eddy covariance techniques and empirical methods. Atmos. Res. 261, 105760.
Chen, C., 1964. The convective instability of the inertia wave and physical analysis of the formation of the typhoon in the early stage. Acta. Met. Sin. 34, 433–442.
Coutts, A.M., Beringer, J., Tapper, N.J., 2007. Impact of increasing urban density on local climate: Spatial and temporal variations in the surface energy balance in Melbourne, Australia. J. Appl. Meteor. Clim. 46, 477–493.
Deardorff, J., 1972b. Parameterization of the planetary boundary layer for use in general circulation models. Mon. Weather Rev. 100, 93–106.
Espinoza-Villar, J., Ronchail, J., Guyot, J., Cochonneau, G., Naziano, F., Lavado, W., De-Oliveira, E., Pombosa, R., Vauchel, P., 2009. Spatio-temporal rainfall variability in the Amazon basin countries (Brazil, Peru, Bolivia, Colombia, and Ecuador). Int. J. Climatol. 29, 1574–1594.
Flores-Rojas, J., Cuxart, J., Piñas-Laura, M., Callañaupa, S., Suárez-Salas, L., Kumar, S., Moya-Alvarez, A., Silva, Y., 2019a. Seasonal and diurnal cycles of surface boundary layer and energy balance in the Central Andes of Perú, Mantaro Valley. Atmosphere 10, 779, http://dx.doi.org/10.3390/atmos10120779.
Flores-Rojas, J., Moya-Alvarez, A., Kumar, S., Martínez-Castro, D., Villalobos-Puma, E., Silva-Vidal, Y., 2019b. Analysis of possible triggering mechanisms of severe thunderstorms in the Tropical Central Andes of Peru, Mantaro Valley. Atmosphere 10 (6), 301–331.
Flores-Rojas, J., Moya-Alvarez, J., Piñas-Laura, M., Kumar, S., Karam, H., Villalobos-Puma, E., Martínez-Castro, D., Silva, Y., 2020. On the dynamic mechanisms of intense rainfall events in the central Andes of Peru, Mantaro valley. Atmos. Res. 248, http://dx.doi.org/10.1016/j.atmosres.2020.105188.
Flores-Rojas, J., Silva, Y., Suárez-Salas, L., Estevan, R., Valdivia-Prado, J., Saavedra, M., Giraldez, L., 2021. Analysis of extreme meteorological events in the Central Andes of Peru using a set of specialized instruments. Atmosphere 12, 408. http://dx.doi.org/10.3390/atmos12030408.
Foken, T., Nappo, C., 2008. Micrometeorology, First Springer-Verlag Berlin Heildelberg.
Garay, O., Ochoa, A., 2010. Primera Aproximación Para La Identificación De Los Diferentes Tipos De Suelo Agrícola En El Valle Del Río Mantaro, First Instituto Geofísico del Perú.
Garreaud, R., 1999. Multiscale analysis of the summertime precipitation over the central Andes. Mon. Wea. Rev. 127, 901–921.
Guo, H., Chen, S., Bao, A., Behrangi, A., Hong, Y., Ndayisaba, F., Hu, J., Stepanian, P., 2016. Early assessment of integrated multi-satellite retrievals for global precipitation measurement over China. Atmos. Res. 176–177, 121–133.
Hobouchian, M., Salio, P., García Skabar, Y., Vila, D., Garreaud, R., 2017. Assessment of satellite precipitation estimates over the slopes of the subtropical Andes. Atmos. Res. 190, 43–54.
Jun, W., Zhigang, W., Shihua, L., Shiqiang, C., Yinhuan, A., Ling, L., 2007. Autumn daily characteristics of land surface heat and water exchange over the loess plateau Mesa in China. Adv. Atmos. Sci. 24 (2), 301–310.
Junquas, C., Takahashi, K., Condom, T., Espinoza, J., Chavez, S., Sicart, J., Lebel, T., 2018. Understanding the influence of orography on the precipitation diurnal cycle and the associated atmospheric processes in the central Andes. Clim. Dyn. 50, 3995–4017.
Kain, J., Fritsch, J., 1993. Convective parameterization for mesoscale models: The Kain Fritsch scheme. The Representation of Cumulus Convection in Numerical Mode. Meteor. Monogr. 24, 165–170.
Keenan, T., Ferrier, B., Simpson, J., 1994. Development and structure of a maritime continent thunderstorm. Meteor. Atmos. Phys. 53, 185–222.
Keenan, T., et al., 2000. The Maritime Continent Thunderstorm Experiment (MCTEX) Overview and some results. Bull. Am. Meteorol. Soc. 81 (10), 2433–2455.
Kiranyaz, S., Avci, O., Abdeljaber, O., Ince, T., Gabbouj, M., Inman, D.J., 2021. 1D convolutional neural networks and applications: A survey. Mech. Syst. Signal Process. 151, 107398. http://dx.doi.org/10.1016/j.ymssp.2020.107398, URL https://www.sciencedirect.com/science/article/pii/S0888327020307846.
Ma, Y., Tang, G., Long, D., Yong, B., Zhong, L., Wan, W., Hong, Y., 2016. Similarity and error intercomparison of the GPM and its predecessor-TRMM multisatellite precipitation analysis using the best available hourly gauge network over the Tibetan Plateau. Remote. Sens. 8, http://dx.doi.org/10.3390/rs8070569.

Manz, B., Páez-Bimos, S., Horna, N., Buytaert, W., Ochoa-Tocachi, B., Lavado-Casimiro, W., Willems, B., 2017. Comparative ground validation of IMERG and TMPA at variable spatiotemporal scales in the tropical andes. J. Hydrometeor. 18 (9), 2469–2489. http://dx.doi.org/10.1175/JHM-D-16-0277.1.

Martínez-Castro, D., Kumar, S., Flores-Rojas, J., Moya-Álvarez, A., Valdivia-Prado, J., Villalobos-Puma, E., Castillo-Velarde, C., Silva-Vidal, Y., 2019. The impact of microphysics parameterization in the simulation of two convective rainfall events over the central Andes of Peru using WRF-ARW. Atmosphere 10, 442–470.

Metek, 2015. MIRA-35c System Description. Meteorologische Messtechnik GmbH.

Monin, A., Obukhov, A., 1954. Basic laws of turbulent mixing in the ground layer of the atmosphere. Tr. Geofiz. Inst. Akab. Nauk. 24, 163–187.

Monteith, J., Unsworth, M., 1990. Principles of Environmental Physics, First, pp 291 Edward Arnold, London.

Oke, T., 1987. Boundary Layer Climates, Second, pp 435 Taylor and Francis Group.

Prakash, S., Mitra, A., Pai, D., AghaKouchak, A., 2016. From TRMM to GPM: How well can heavy rainfall be detected from space? Adv. Water Resour. 88, 1–7.

Prueger, J., Kustas, W., 2005. Aerodynamic Methods for Estimation Turbulent Fluxes, First USDA-ARS / UNL Faculty, 1394.

Raman, S., Niyogi, D.S., Prabhu, A., Ameenullah, S., Nagaraj, S.T., Kumar, U., Jayanna, S., 1998. VEBEX: Vegetation and surface energy balance experiment for the tropics. Proc. the Indian Acad. Sci. - Earth Planet. Sci. 107 (1), 97–105.

Rouse, W., Oswald, C., Binyamin, J., Blanken, P., Schertzer, W., Spence, C., 2003. Interannual and seasonal variability of surface energy balance and temperature of central great slave lake. J. Hydrometeor. 4, 720–730.

Satyanarayana, A., Sultana, Sabiha, Narayana Rao, T., Satheesh Kumar, S., 2014. Evaluation of atmospheric turbulence, energy exchanges and structure of convective cores during the occurrence of mesoscale convective systems using MST radar facility at Gadanki. Atmos. Res. 143, 198–215.

Schultz, P., 1995. An explicit cloud physics paramterization for operational numerical weather prediction. Mon. Weather Rev. 123, 3331–3343.

Sellers, P.J., Mintz, Y., Sud, Y., Dalcher, A., 1986. The designing of a simple bio-sphere model (SiB) for use within general circulation model. J. Atmos. Sci. 43, 505–531.

Sharifi, E., Steinacker, R., Saghafian, B., 2016. Assessment of GPM-IMERG and other precipitation products against gauge data under different topographic and climatic conditions in Iran: Preliminary results. Remote. Sens. 8,135, http://dx.doi.org/10.3390/rs8020135.

Silva, Y., Takahashi, K., Chavez, R., 2008. Dry and wet rainy seasons in the mantaro river basin (Central Peruvian Andes). Adv. Geosci. 14, 261–264.

Silva, Y., Trasmonte, G., L., G., 2010. Variabilidad De Las Lluvias En El Valle Del Mantaro Memoria Del Subproyecto: Pronóstico Estacional De Lluvias Y Temperatura En La Cuenca Del Río Mantaro Para Su Aplicación En La Agricultura, Primera Fondo Editorial CONAM-Instituto Geofísico del Perú.

Su, Z.B., 2002. The surface energy balance system (SEBS) for estimation of turbulent heat fluxes. Hydrol. Earth Syst. Sci. 6 (1), 85–99.

Tan, J., Petersen, W., Tokay, A., 2016. A novel approach to identify sources of errors in IMERG for GPM ground validation. J. Hydrometeor. 17, 2477–2491.

Tang, G., Zeng, Z., Long, D., Guo, X., Yong, B., Zhang, W., Hong, Y., 2016. Statistical and hydrological comparisons between TRMM and GPM Level-3 products over a midlatitude basin: Is Day-1 IMERG a good successor for TMPA 3B42v7? J. Hydrometeor. 17, 121–137.

Thompson, C., Beringer, J., Chapin, F.S.I., McGuire, A.D., 2004. Structural complexity and land-surface energy exchange along a gradient from arctic tundra to boreal forest. J. Veg. Sci. 15, 397–406.

Tyagi, B., Satyanarayana, A.N.V., 2015. Delineation of surface energy exchanges variations during thunderstorm and non-thunderstorm days during pre-monsoon season. J. Atmos. Sol.-Terr. Phys. 122, 138–144.

Tyagi, B., Satyanarayana, A.N.V., Kumar, M., Mahanti, N., 2012. Surface energy and radiation budget over a tropical station: An observational study. Asia- Pac. J. Atmospheric Sci. 48 (4), 411–421.

Valdivia, J., Scipion, D., Milla, M., Silva, Y., 2020. Multi-instrument rainfall-rate estimation in the peruvian central andes. J. Atmos. Ocean. Technol. 37 (10), 1811–1826, URL https://doi.org/10.1175/JTECH-D-19-0105.1.

Venalainen, A., Solantie, R., Laine, V., 1998. Mean long term surface energy balance components in Finland during the summertime. Boreal Environ. Res. 3, 171–180.

Villalobos-Puma, E., Martinez-Castro, D., Flores Rojas, J., Saavedra, M., Silva Vidal, Y., 2020. Diurnal cycle of raindrops size distribution in a valley of the Peruvian Central Andes. Atmosphere 11, http://dx.doi.org/10.3390/atmos11010038.

Xue, M., Droegmeier, K., Wong, V., 2000. The Advanced Regional prediction system (ARPS)-A multi-scale nonhydrostatic atmospheric simulation and prediction model. Part I:Model dynamics and verification. Meteorol. Atmos. Phys. 1, 1–45.

Xue, M., Droegmeier, K., Wong, V., 2001. The Advanced Regional prediction system (ARPS)-A multi-scale nonhydrostatic atmospheric simulation and prediction model. Part II: Model physics and applications. Meteorol. Atmos. Phys. 76, 143–165.

Xufeng, W., Mingguo, M., 2009. Characteristic of maize land energy balance during maize growing period. Ext. Abstr. Present. Int. Conf. Land Surf. Radiat. Energy Budgets: Obs. Model. Anal. March, 18–20.